AN ABSTRACT OF THE DISSERTATION OF

Guangxin Wang for the degree of Doctor of Philosophy in Electrical and Computer Engineering presented on December 08, 2022.

Title: Environment-adaptive RF Sensing with Transferable ANN Features

Abstract approved: _____

Huaping Liu

Radio frequency (RF) sensing arises as a promising option for enabling the internet of things (IoT) applications that transform our life into a world of smart homes, smart cities, and smart industries. The innovation of IoT reveals the benefits of RF sensing across cost, pervasiveness, unobtrusiveness, and privacy. However, challenges like interference and multipath are underway in realizing those promises. Furthermore, crucial studies demonstrate the trade-offs in accuracy, accessibility, power consumption, and many other factors for undertaking RF sensing. This dissertation presents a set of studies, including RF channel model characterization, the design of a novel RF sensing system for indoor localization, and the environmental impact of RF exposure in such systems. The first part covers a use case of measurement-based RF channel modeling in a challenging environment. The second part introduces an environment-adaptive RF sensing system for indoor localization that consists of 1) a dynamic phase calibration de-noising method, and 2) The implementation of a localization system that utilizes an artificial neural network (ANN) with transferable features. Lastly, a collaboration work that explores the potential impact of RF radiation and how RF exposure could affect human health.

Environment-adaptive RF Sensing with Transferable ANN Features

by

Guangxin Wang

A DISSERTATION

submitted to

Oregon State University

in partial fulfillment of
the requirements for the
degree of

Doctor of Philosophy

Presented December 08, 2022
Commencement June 2023

Doctor of Philosophy dissertation of Guangxin Wang presented on December 08, 2022.

APPROVED:

Major Professor, representing Electrical and Computer Engineering

---

Head of the School of Electrical Engineering and Computer Science

---

Dean of the Graduate School

I understand that my dissertation will become part of the permanent collection of Oregon State University libraries. My signature below authorizes release of my dissertation to any reader upon request.

Guangxin Wang, Author

ACKNOWLEDGEMENTS

I would like to express my deepest gratitude to my major advisor Prof. Huaping Liu. I could not have undertaken my Ph.D. work without his magnanimous mentorship and invaluable patience. I'm extremely grateful to my committee members Prof. Tejasvi Anand, Prof. Eduardo Cotilla-Sanchez, Prof. Jinsub Kim, and Prof. William Warnes, who generously provided their guidance and expertise.

I am grateful to my friends, team members, and colleagues, who impacted and inspired me throughout my life and work in Corvallis. Also, thanks to all the community members at EECS and OSU who provided enormous help and support.

Lastly, I am deeply indebted to my parents and in-laws, especially my beloved wife and son, for all the happiness and love they have given me. Their belief in me has kept my spirits during this journey. This endeavor would not have been possible without all their patience and unconditional support.

TABLE OF CONTENTS

TABLE OF CONTENTS (Continued)

LIST OF FIGURES

LIST OF FIGURES (Continued)

LIST OF TABLES

Chapter 1: Introduction

The emerging Internet of things (IoT) paradigm has revolutionized wireless communication, enabling sensor and device connectivity via networks. Radio frequency (RF) sensing is one of the techniques that provide innovative solutions to various IoT applications related to smart homes, smart cities, and smart industries. IoT devices sense the surroundings of physical objects and interpret information from them. Smart sensors and devices emit RF signals (e.g., WiFi, Bluetooth, Ultra-wideband (UWB), and 4G/5G cellular) through the IoT environment. Any object within those spaces, such as humans, equipment, furniture, and walls, will reflect, refract, diffract, and scatter the RF signals. Thus, RF propagation can be analyzed from channel modeling and characterization to extract information like an object's presence, movement, position, and activity. This technique is called RF sensing, which has gained increasing interest due to its low-cost, pervasiveness, and unobtrusiveness [1, 2].

The following sections are organized as 1.1) summarizing the RF channel modeling and characterization that further discussed in Chapters 2, 1.2) explaining the artificial neural network (ANN) framework for RF sensing that showcased in Chapters 3 and 4, and 1.3) discussing RF emission from wireless devices that case studied in Chapters 5.

1.1 RF Channel Modeling and Characterization

The first step to extracting meaningful information from the captured RF signal is understanding the characteristics of RF propagation. RF radiates from the transmitter (Tx)

antenna and is received by the receiver (Rx) antenna. The RF propagation characteristics are dictated by frequency, wavelength, and amplitude. Depending on the technology and the part of the world the system is being deployed, regulatory bodies, e.g., Federal Communications Commission (FCC) in the US, will govern and allocate the frequencies and radio bands.

Regardless of the frequency, the same propagation characteristics apply. RF path modeling describes the behavior of RF radiation from the point of transmission as the signal travels through the environment. Channel modeling describes the over-the-air environment in wireless links. Traditional model-based RF sensing methods engage mathematical models to describe the behavior of RF propagation. Model-based approaches oversimplify the case and fail in the complex real-world environment. For example, multipath fading and interference can make the models extremely complicated. However, propagation and channel modeling analysis is essential in understanding how electromagnetic waves incur losses and delay from a transmitter to a receiver in different scenarios [3].

1.2 ANN Framework for RF Sensing

On wireless transceivers, the data is modulated on one end, transmitted over RF links, and demodulated on the other end. During signal transmission, time of flight (ToF), time difference of flight (TDoF), angle of arrival (AoA), angle of departure (AoD), received signal strength indicator (RSSI), and channel state information (CSI) can be accessed at the physical layer for RF sensing. Machine learning methods can represent data and extract features from the physical layer data. An ANN framework can leverage deep learning to process high-dimensional data and solve high-level RF sensing problems. Furthermore, novel learning-based RF sensing ANNs distill cross-domain and environment-independent

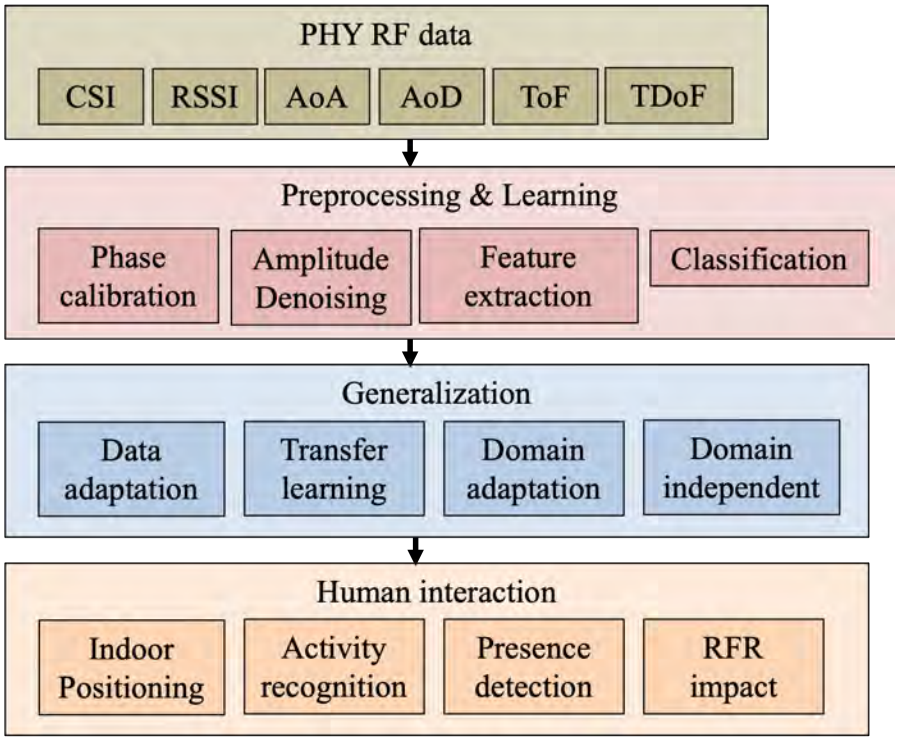

Figure 1.1: The conceptual ANN Framework for RF Sensing

knowledge from the training dataset, leading to better generalizability. The conceptual ANN framework (Fig.1.1) confines four segments: physical (PHY) layer RF signals, machine learning schemes, learning generalization, and RF sensing application.

1.2.1 PHY Layer and RF Signals

For RF sensing, the PHY layer can use various signals such as WiFi [4], Bluetooth [5], UWB [6, 7], radio-frequency identification (RFID), and millimeter wave (mm-Wave)[8]. WiFi is a technology that uses radio waves to provide network connectivity for devices based on the 802.11 standards. WiFi provides information for RF sensing without

additional infrastructures. The most commonly extracted data from WiFi are RSSI and CSI. RSSI provides coarse-grained signal intensity information, and CSI has the fine-grained characterization of an Orthogonal Frequency-Division Multiplexing (OFDM) channel. WiFi also utilizes an antenna array to exploit multiple-input and multiple-output (MIMO) that depicts the CSI of each subcarrier between every Tx-Rx antenna pair. RF sensing exploiting WiFi CSI has emerged as CSI can be obtained from WiFi devices with custom drivers or modified firmware [2].

1.2.2 Machine Learning Schemes

Before feeding the RF data into ANNs, preprocessing is demanded to remove the data imperfection and accelerate the learning process. Filtering separates signal and noise by transforming the RF signals into another domain. Additional de-noising methods may be needed depending on system complexity and accuracy. Data preprocessing, like dimension reduction, helps with a more robust model to not overfit the data.

The RF data is ready for feature extraction after preprocessing. Conventionally model-based approaches compute the target's position information and exploit them to further spatial features. Moreover, deep learning networks often skip these intermediate steps and extract spatial features using ANNs.

Type of ANN includes Convolutional Neural Network (CNN), Recurrent Neural Network (RNN), and Long Short-Term Memory Network (LSTM). CNN encodes the prior knowledge of translation invariance into itself. The convolution operation gives a constant activation value regardless of the feature location; on the other hand, the pooling layer downsamples the feature map to make it insensitive to the change of feature location. CNN takes orders of magnitude and is well adapted for spatial feature extractor RNN

takes the current value as input and past inputs, which are stored as hidden states of the RNN nodes. The nodes form a directed graph closely related to the time sequence, displaying temporal behavior. Compared to CNN, RNN can process input series of any length, and the complexity of the model does not increase with the input size. Therefore RNN is chosen for extracting temporal features. LSTM maintains information in memory for more extended periods. LSTM solves the vanishing and exploding gradient problem of long RNN by introducing forget gate, input gate, and output gate into the network. The gates work together to decide how much information will be thrown away, kept in the node, taken as input, and used as output. By controlling the flow of information, LSTM outperforms RNN when dealing with long dependencies.

1.2.3 Learning Generalization

Above mentioned ANNs work for RF sensing applications. However, it suffers from domain shift and data scarcity. Domain shift indicates the performance drops when the environment changes. Data scarcity means that not sufficient training data is collected. Those two causes are related: domain shift entails a laborious process of collecting and labeling new data. Some studies tried solving these challenges by handcrafting domain-independent features (HCF). However, HCF depends on prior information such as location, position, and environmental factors. Manually obtaining those data incurs another time and labor-consuming process.

A generalization layer on top of ANNs extends the capability of the machine learning process that is trained for a single domain. By employing corresponding generalization logic (e.g., knowledge transfer and data generation), it generalizes the ML model from the training domain to the target domains. As a result, deep learning models for RF sensing

systems can be trained once, adaptive to other environments, and provide more extensible services. Different techniques can be used in the generalization layer, including:

1) Generative Adversarial Network: Generative Adversarial Network (GAN) helps generalize from small training datasets to larger, more universal datasets. GAN is a two-player game in which the generative network ($\mathcal{G}$) and the discriminative network ($\mathcal{D}$) are pitted against each other. During training, $\mathcal{G}$ generates fake data conforming to the distribution of a given dataset, trying to confuse $\mathcal{D}$; while $\mathcal{D}$ the classifier, tries to discriminate fake data generated by $\mathcal{G}$ and true training data. After iterations, the data generated by $\mathcal{G}$ is good to beat $\mathcal{D}$, which can be used to extend the dataset. $\mathcal{G}$ helps generate WiFi fingerprints for indoor localization. By extending the dataset, the RF sensing system achieves a faster convergence time and requires less human effort. GAN can also recover lost fingerprints for continuous localization and tracking.

2) Adversarial Domain Adaptation: Adversarial domain adaptation is an approach to generalizing from one domain to another. It aims to learn models that transform different domains into a common feature space. It is similar to GAN mentioned above, where there is a competition between $\mathcal{G}$ and $\mathcal{D}$. The difference is that in GAN, the output of $\mathcal{G}$ is of interest, whereas in adversarial domain adaptation, we are interested in learning features invariant across domains by playing the min-max game. Adversarial domain adaptation is used to achieve environment-independent activity recognition by employing it to transform and adapt the RF data tensor to new environments for pose estimation.

3) Transfer Learning: Transfer learning works by fine-tuning pre-trained models to handle similar tasks since these tasks often share common knowledge. For example, the trained weights of the first several layers of neural networks can be reused across different tasks since the layers capture input features independent of specific tasks. We can transfer this knowledge and fine-tune the rest of the model, therefore adapting the model to the

new task with few samples and low cross-domain training cost. In the generalization layer, the idea is to transfer knowledge from the source domain to the target domain. Transfer learning can achieve accurate cross-domain gesture classification and leverage the generalizability of transfer learning to predict previously unseen environments.

1.2.4 RF Sensing Applications

The development of RF sensing has enabled many interesting IoT applications. The growing need for location-based services (LBS) requires accurate and robust solutions RF sensing provides a solution for indoor localization where GPS fails to reach. Furthermore, data-driven approaches are increasingly employed with RF sensing for localization purposes. As an example, RF fingerprinting matches measured features extracted from RSSI and CSI to predefined ones on an RF mapping. However, this method requires lots of fingerprints to cover the space. Also, the performance is affected by the high variability of RF signals caused by multipath fading and interference. Therefore, deep learning fully explores RF data and extracting deep features, irrelevant information can be stripped while useful spatial features retained, and localization accuracy can be potentially improved.

1.3 RF Emission from Wireless Devices

Wireless devices like cell phones are regarded as the fundamental components of IoT and have been commonly used in people's daily lives. The involvement of RF sensing systems improves how humans live, but as such technologies grow, RF radiation (RFR) exposure has been a concern for the public, health authorities, and researchers [9]. Knowledge of the RFR on or inside the human body is critical in understanding the health impact of

RF devices and signals. However, the physical experiment is extremely difficult for the human body. In the last part of this dissertation, collaborative work with the Department of Environmental and Molecular Toxicology systematically used zebrafish as a surrogate model to study how RFR might affect early development. A testing chamber is designed specifically for 5G cellular exposure. With this established robust in vivo testing platform, the changing RFR exposure scenarios are positioned to be modeled and measured, and their biological effects to address concerns about broadband technology and human health.

Measurement-based Channel Modeling for mmWave Wireless Links in Enclosed Server Platforms

Guangxin Wang, Kai Zhan, Telesphor Kamgaing, Rahul Khanna, Huaping Liu, and Arun Natarajan

IEEE Radio and Wireless Symposium (RWS)
Wireless Architecture & Modeling
Phoenix, AZ
15-18, January 2017

Chapter 2: Measurement-based Channel Modeling for mmWave Wireless Links in Enclosed Server Platforms

Abstract: The large available bandwidths, demonstrations of fully-integrated silicon transceivers and small physical antenna size make mm-wave frequencies attractive for wireless links within a server chassis. In this paper, we focus on studying the feasibility of a mm-wave wireless link within a commercial microserver chassis for high data-rate links and for management and monitoring. Such servers have reflective metal walls and are densely populated with microserver boards that create barriers for mm-wave signals. A custom test setup is used for in-situ channel measurements at 57GHz for both line-of-sight (LOS) and non-line-of-sight (NLOS) links across different TX-RX separations. The NLOS links show RMS delay spread of 32ns@50% CDF (∼200ns@90% CDF) with path loss >55dB, indicating a challenging environment for low-power high-speed links. Therefore, a modified chassis with 10mm headroom between the top of the boards and chassis cover is proposed. Measurements show that such an environment can make the targeted wireless links feasible with ∼35dB loss, and RMS delay spread of 14ns@50% CDF (∼20ns@90% CDF).

2.1 Introduction

Wireless links within server chassis are useful for reconfigurable, short-range routing and for management and monitoring without complex cable routing [10]. The large

available spectrum at mm-wave frequencies, such as 60GHz, and the small antenna size makes it attractive to implement short-range, high data rate wireless links within chassis, particularly using fully-integrated mm-wave transceivers [11]. The objective of this paper is to study propagation properties of mm-wave wireless links in a microserver chassis and use measurement-based channel models to evaluate the feasibility of wireless links within the enclosure. mm-Wave propagation channels for such highly-reflective enclosed environments have been studied using ray-tracing simulations [12] and measurements in metal enclosures emulating target systems [13]. Ray-tracing numerical simulations underestimate the reflective/multi-path effects of the metallic environments, particularly in a microserver chassis densely populated with server boards. The proposed dense multipath environment also differs from the measurements in [13], that consider an enclosure that is not densely populated. In this paper, we present line-of-sight (LOS) and non-line-of-sight (NLOS) channel measurements in microserver chassis. Notably, the measurements here include a typical planar patch antenna at both ends to evaluate the feasibility of a short-range link within the commercial microserver chassis.

2.2 mmWave Channel Measurement Setup

The microserver chassis, measuring $534 \times 178 \times 127$ mm^3, is shown in Fig. 2.1(a)(b). The original metal chassis cover is replaced by a custom 6061 aluminum alloy cover, which has 8×6 slots to enable in-situ measurements using connectorized V-band patch antennas across different TX-RX locations. Measurements are performed across different slot combinations in Fig. 2.1(b), including both LOS and NLOS scenarios. The (x, y) index for each position is based on Fig. 2.1(b). At each position, as shown in Fig. 2.2, four different insertion depth, 5mm, 50mm, 70mm and 100mm, are measured. In our approach,

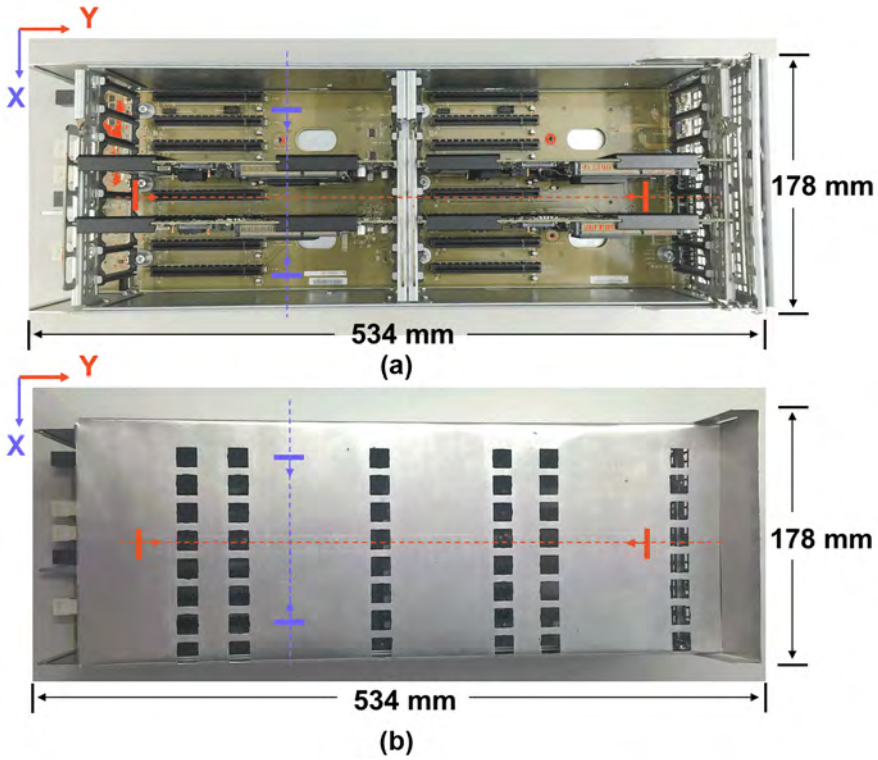

Figure 2.1: Microserver chassis with server boards - (a) with cover removed, (b) with custom-machined cover with slots.

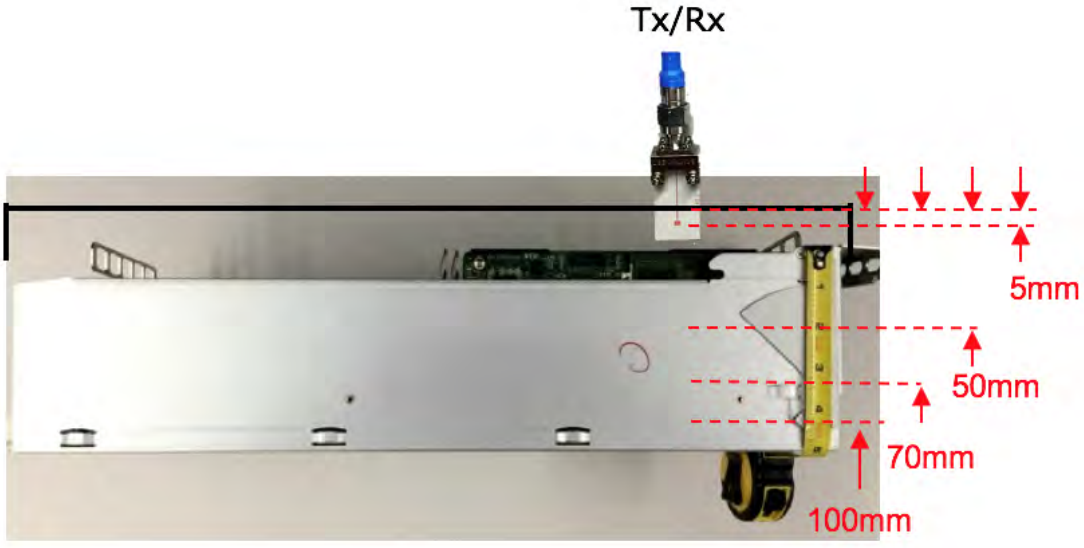

Figure 2.2: Channel measurement across insertion depths for each antenna position.

a Keysight network analyzer (PNA N5227A) is used to measure the S-parameters (S_{11}, S_{22}, S_{21}, and S_{12}) up to 67GHz. S_{21}, which represents the power transferred from TX to RX, is extracted for subsequent CIR calculations [14], [15]. The reflection coefficient S_{11} is acquired to analyze the input matching of the antenna. In the following measurements, the channel includes the antenna at both ends. Fig. 2.3(a)(b) shows the setup where two antennas are inserted into the chassis through the slots in the cover for the in-situ test. Input match of the antenna and a representative transfer function for LOS is shown in Fig. 2.3(c).

Next, measurements are divided into three scenarios to understand LOS and NLOS channel characteristics.

2.2.0.1 Scenario 1: LOS, without microserver boards

There is no microserver board obstructing the TX and RX antennas. This corresponds to LOS measurements inside the empty metal chassis, similar to [13].

2.2.0.2 Scenario 2: LOS, with microserver boards

With the original metal cover, there is no vertical headroom between the top of the microserver boards and the cover. However, as shown in Fig. 2.2, the custom cover is designed to provide variable headroom. Four 210×120 mm^2 microserver boards are installed in the server chassis. Scenario 2 measurements correspond to 10mm space between the top of microserver boards and the cover. In this setup, even with four microserver boards installed, there can be a LOS link in the empty headroom space if the TX and RX antennas are inserted 5mm into the chassis.

2.2.0.3 Scenario 3: NLOS, with microserver board

The boards can block the LOS path if the TX-RX are separated by them. Channel measurements are performed to evaluate NLOS link feasibility in the presence of such barriers.

2.3 Measurement Results

2.3.1 Large-scale fading characteristics: path loss

2.3.1.1 Depth dependence

Fig. 2.4(a) shows the measured S_{21} of the link at various insertion depths in Scenario 1, at the same 80mm TX-RX separation. The highest S_{21} is similar for different antenna depths implying that insertion depth does not affect path loss significantly. Fig. 2.4(b) shows the measured S_{21} in Scenarios 2 and 3. Notably, the path loss at 5mm depth (Scenario 2) is >10dB better than NLOS in Scenario 3 with considerable less multipath fading as well. However, in NLOS cases, the loss is not significantly depth-dependent.

2.3.1.2 Distance dependence

The path loss (dB) is expressed as

$$P_L(d) = P_L(d_0) + \alpha \cdot 10\log_{10}(d/d_0) + \chi \tag{2.1}$$

where d_0 is a reference distance (20 mm), α is the path-loss exponent, and χ is a zero-mean Gaussian random variable. Fig. 2.4(c) shows path loss measurements in Scenarios 2 and 3 that represent practical link scenarios. Using minimum mean square error fitting, the pass loss in dB is given by

$$P_L(d)_{\text{LOS, scenario 1}} = 29.62 + 1.66 \cdot 10\log_{10}(d) \tag{2.2a}$$

$$P_L(d)_{\text{LOS, scenario 2}} = 28.12 + 1.49 \cdot 10\log_{10}(d) \tag{2.2b}$$

$$P_L(d)_{\text{NLOS, scenario 3}} = 57.62 + 0.096 \cdot 10\log_{10}(d). \tag{2.2c}$$

Measurements show that path loss parameters $P_L(d_0)$ are very close in Scenarios 1 and 2, and have a weak dependence on distance. However in the NLOS condition in Scenario 3 (Fig. 2.4(c)) the path loss curve is relatively flat since the dominant path is blocked.

2.3.2 Small-scale fading characteristics: RMS delay spread

In this work, the squared-magnitude of the CIR is referred to as the power delay profile (PDP). Fig. 2.5 shows the PDP measured for the 80mm TX-RX separation in Scenarios 2 and 3. In Scenario 2, at the same 80mm TX-RX separation and 5mm depth, the LOS case has a smaller RMS delay spread (RDS), while Scenario 3 leads to significantly different PDP across depths.

Delay spread is an important channel characteristic since a large delay spread introduces more inter-symbol interference (ISI), limiting data rates. In the following, mean delay ($\overline{\tau}$), maximum excess delay and RDS (τ_{rms}), for a multipath channel are defined as per [16]. Fig. 2.6 shows the empirical cumulative distribution function (CDF) of the RDS

Table 2.1: Channel RMS delay spreads across scenarios.

	Scenario 1	Scenario 2	Scenario 3
τ_{rms} (ns)	3.6032	14.4552	32.1202

values for Scenarios 2 and 3. The mean RDS values are larger than prior measurements due to the inclusion of the microserver boards within chassis [13]. We obtained values of 14.4ns for Scenario 2, and 32.1ns for Scenario 3 at 50% CDF demonstrating the benefit of the link through the headroom. Note that the RDS at 90% CDF is much larger for scenario 3. The channel coherence bandwidth, as well as the frequency correlation function, can be calculated from the RDS, which can be used to assess the frequency selectivity for a given bandwidth [13].

Measurements also show a nearly linear relationship between $\overline{\tau}$ and τ_{rms}, indicating that the $\overline{\tau}$ and τ_{rms} are highly correlated. This can be used for predicting τ_{rms} [17]. Summary of measured τ_{rms} values for Scenarios $1-3$ is shown in Table 2.1. The wide RDS distribution and >55dB path loss in Scenario 3 limits data rate and also increases the required TX power, leading to higher power consumption. The ∼20dB lower loss and lower RDS leads us to propose microserver chassis with ∼10mm headroom between the boards and the cover to enable high-speed, lower-power short-range wireless links without the use of multi-hop links from board to board.

2.4 Conclusion

This paper presents the channel model for mm-wave wireless links within a microserver chassis. The model is derived from actual S-parameter measurements using a connectorized mm-wave patch antenna. Path loss models, power delay profiles, and RMS delay spreads are obtained for both LOS and NLOS conditions. The measured environment is

highly reflective. Based on measurements, we propose creating 10mm headroom between the sidewalls and cover of the chassis to establish LOS links between TX and RX in order to achieve better system performance.

Acknowledgment

The authors acknowledge Intel for providing the microserver chassis and project funding and H. Braunisch and G. Dogiamis (Intel) for technical discussions.

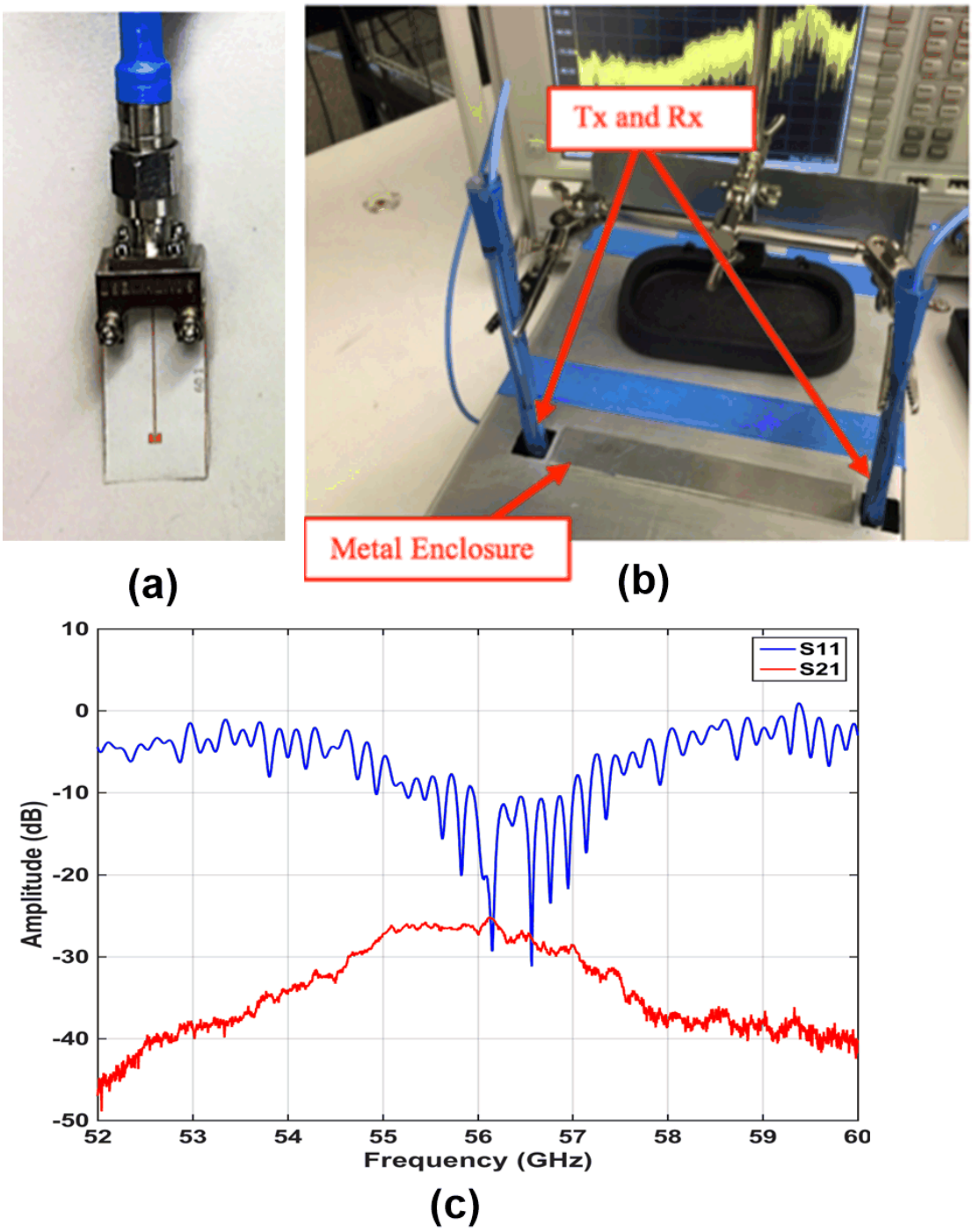

Figure 2.3: (a) Connectorized mm-wave rectangular patch antenna (center frequency: 56GHz), (b) inserted through slots in the chassis cover for different location and depths, (c) measured antenna input matching and transfer function for an LOS link.

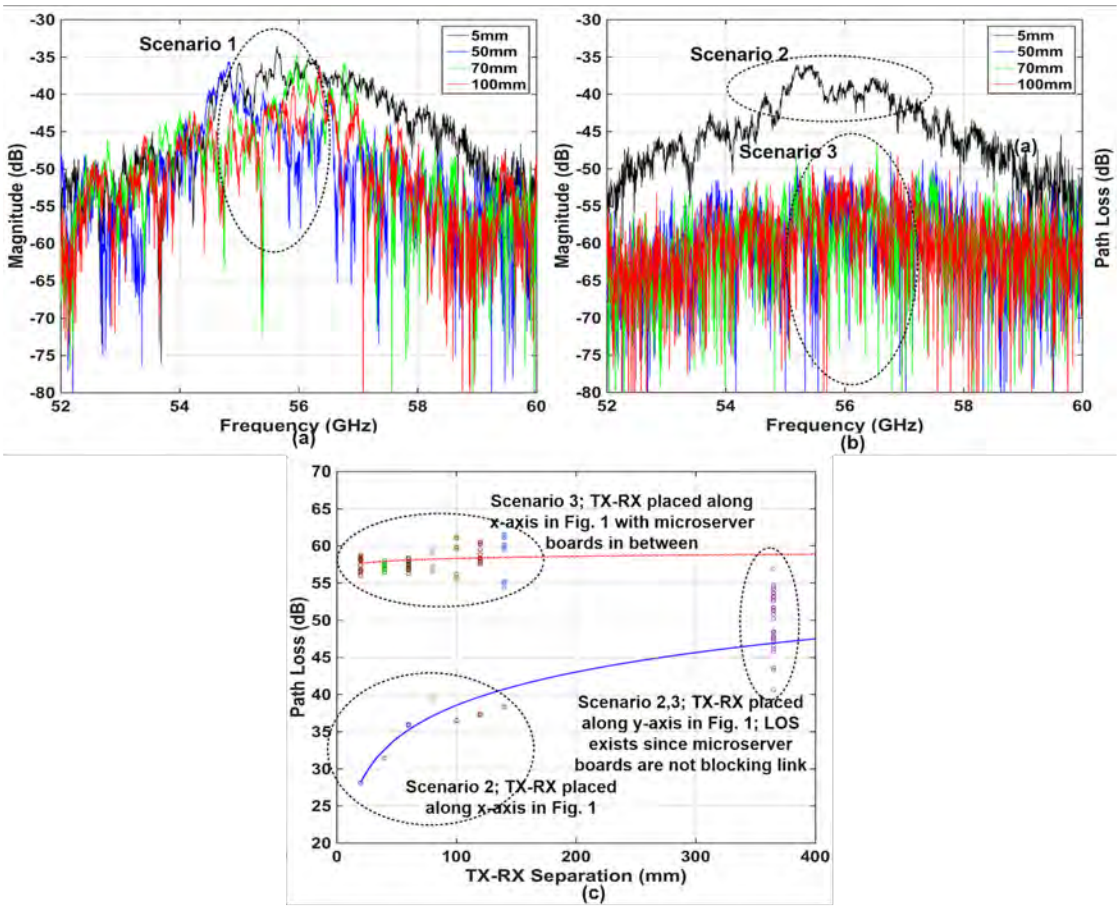

Figure 2.4: Measured channel frequency response with the 56GHz patch antenna at 80mm TX-RX separation and different insertion depth (Fig. 2.2) for (a) Scenario 1, (b) Scenarios 2 & 3. (c) Measured path loss across TX-RX separation in Scenarios 2 and 3.

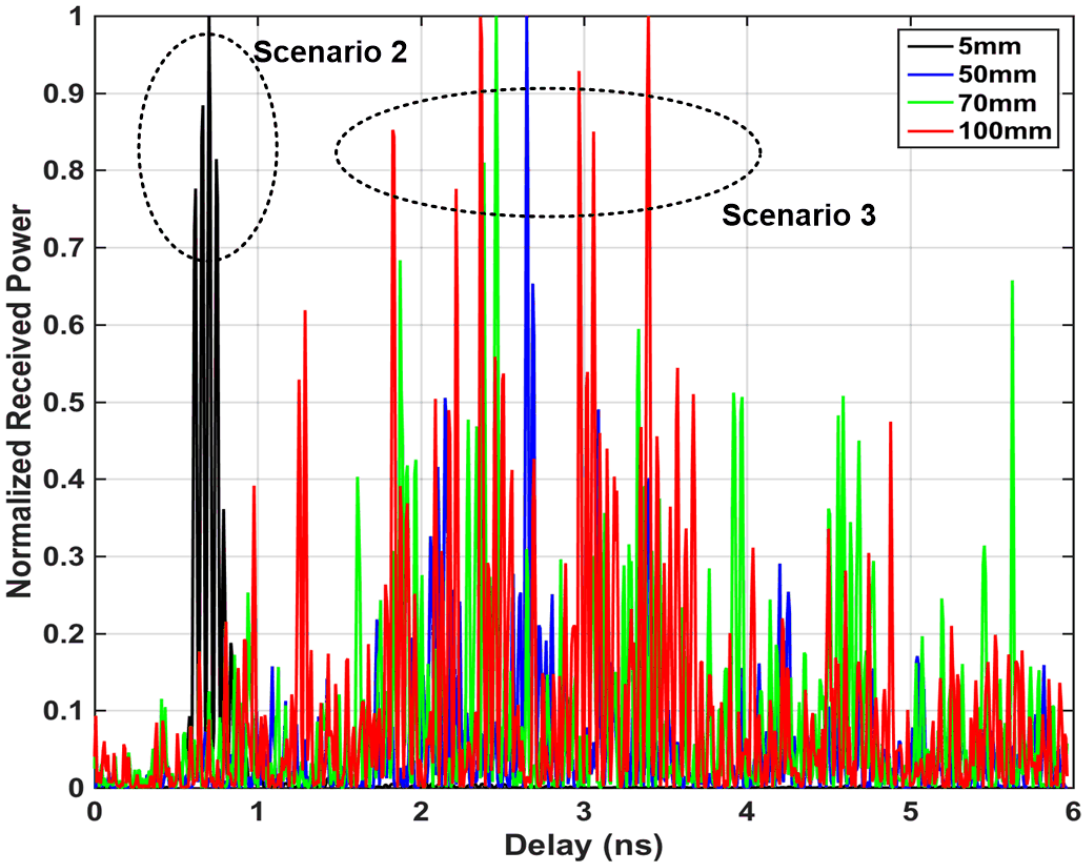

Figure 2.5: Measured PDP in Scenarios 2 and 3.

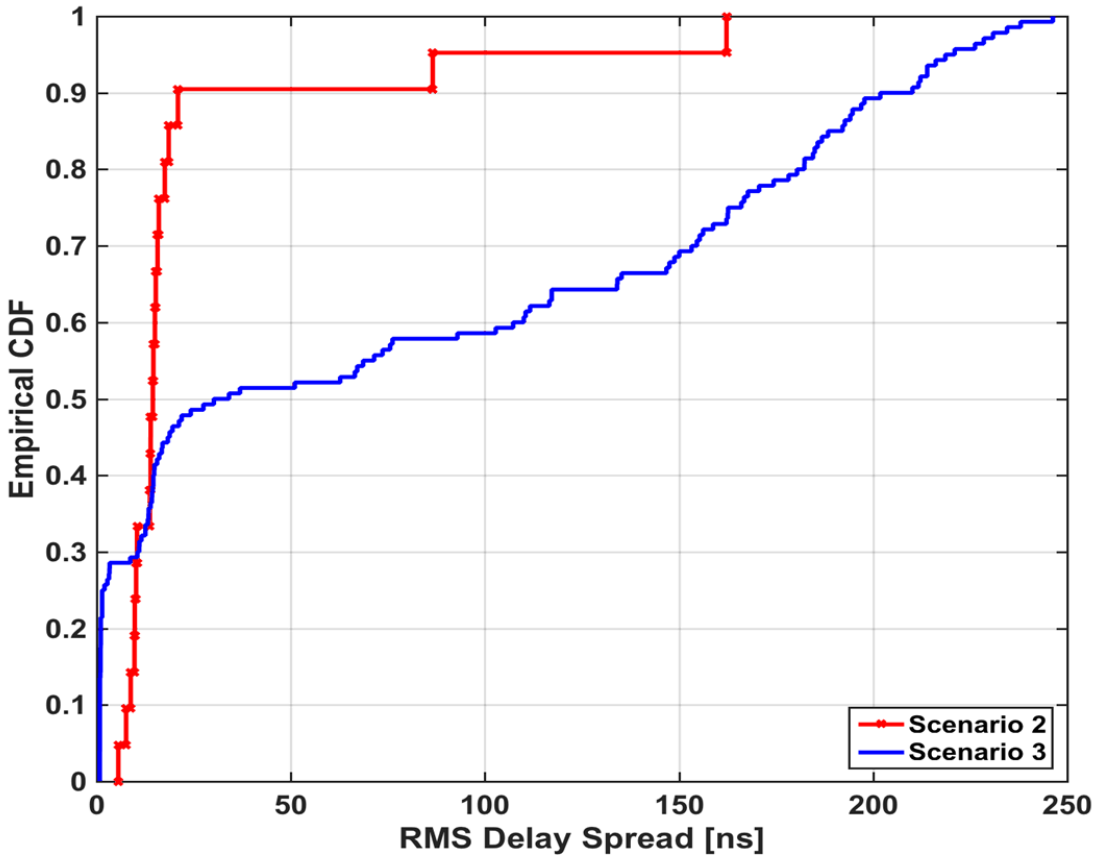

Figure 2.6: Measured RDS distribution in Scenarios 2 and 3.

Dynamic Phase Calibration Method for CSI-based Indoor Positioning

Guangxin Wang, Arash Abbasi, and Huaping Liu

Proc. of IEEE 11th Annual Computing and Communication Workshop and Conference (CCWC)

Artificial Intelligence and Machine Learning

Las Vegas, NV

27-30, January 2021

Chapter 3: Dynamic Phase Calibration Method for CSI-based Indoor Positioning

Abstract: The demand for location-based services (LBS) increases significantly with the development of smart devices. Their built-in WiFi capability makes WiFi-based approaches essential for a range of indoor positioning applications. In such LBS systems, accessing received signal strength indicator (RSSI) and finer-grained channel state information (CSI) is enabled by modifying commodity WiFi devices. Additionally, multiple-input and multiple-output (MIMO) and orthogonal frequency-division multiplexing (OFDM) provide the spatial and frequency diversity to build the fingerprint database with CSI. However, due to hardware and environmental impacts, such systems suffer from phase errors and fingerprint noise. In this paper, a novel phase calibration method is proposed to reduce the fingerprint noise and improve the accuracy of CSI-based indoor positioning systems. The CSI phase of each subcarrier is extracted from the WiFi access points in a multi-antenna wireless network. First, the phase offset is calculated through the conventional method that uses a linear transformation to remove phase errors. Then, a dynamic phase calibration method is introduced to compensate for the phase offset by tracking the anomalous phase difference between each CSI sample and neighboring subcarrier. Finally, a machine learning algorithm is trained to estimate the target position. The performance of the proposed algorithm is investigated by evaluating the prediction rate from a margin of error (MoE) model and calculating the average distance error between the predicted grid and ground truth. Experimental results show the dynamic

phase calibration method outperforms the conventional linear transformation calibration method by a higher prediction rate and improves the average position accuracy.

3.1 Introduction

Wireless positioning systems play a significant role in various location-based services (LBS) such as location awareness, navigation, and object tracking. The demand for such services is envisioned to increase drastically as smart applications developing. For outdoor positioning services, global navigation satellite systems (GNSS) like GPS, GLONASS, Galileo, and Beidou provide a reliable solution. The aforementioned GNSS systems are incapable of providing accurate positioning services for most indoor scenarios. However, most human activities occur in indoor environments [18]. For indoor positioning, various techniques such as ultra-wide band (UWB) [6, 7], Bluetooth [5], radio-frequency identification (RFID) [19], and WiFi [4] have been proposed in the past two decades. Among them, WiFi-based approaches have attracted widespread interest as ubiquitous, low-cost solutions for indoor applications. WiFi-based indoor positioning systems can be categorized into two types: 1) signal propagation approaches, in which propagation parameters such as time of arrival (ToA) [20, 21], time difference of arrival (TDoA) [22–25], and angle of arrival (AoA) are measured to estimate the target location; and 2) fingerprinting-based approaches, in which a database is maintained with certain fingerprint features, including received signal strength indicator (RSSI) and channel state information (CSI) to match the target's position. One advantage of fingerprint-based systems is that they are device-free, meaning they can detect an object's position without requiring the object to carry additional hardware.

In the WiFi 802.11 protocol, multiple-input and multiple-output (MIMO) and orthog-

onal frequency-division multiplexing (OFDM) provide the spatial and frequency diversity, enabling the receiver to access channel information. RSSI is widely used in fingerprint-based schemes because of the simplicity and accessibility to extract the signal strength information. RSSI-based fingerprint method for indoor positioning is introduced in [26] and [27], where the target's position is investigated using a probability model from the RSSI measurements. However, RSSI only provides coarse-grained channel information from the medium access control (MAC) layer. Because RSSI measures the average value of the received data packet, it is sensitive to environmental variations. Study shows that RSSI-based systems achieve an average accuracy of 2 to 4 meters [28]. In contrast, CSI captures fine-grained channel information measured by OFDM subcarriers from the physical (PHY) layer that contains the frequency diversity of the channels. Therefore, the CSI-based method outperforms the RSSI-based approach in positioning accuracy, and system stability [4] [29]. Moreover, CSI approaches are capable of detecting channel fading caused by environmental changes and multipath reflections [30]. In general, comparing to the RSSI-based approach, the finer granularity and low susceptibility to environmental factors make the CSI-based approach a better candidate in fingerprinting systems.

Different features such as phase, amplitude, and the hybrid of both have been investigated in CSI-based fingerprint systems. In [31] and [32], the frequency diversity of OFDM subcarriers is explored, and the sum of CSI amplitudes is used to create the fingerprint database. However, multipath fading limits the accuracy and robustness of this CSI amplitudes approach. The CSI phase is combined with its amplitude to improve performance. FIFS [33] and CSI-MIMO [34] utilize both the CSI amplitude and phase as fingerprints and adopt a probabilistic model to determine the target location without proper phase calibration. To compensate for the phase offset caused by the lack

of synchronization between the transmitter and receiver, PinLoc [35], and DeepFi [36] use linear transformation to calibrate the CSI phase. A phase sanitization method is also proposed in PhaseFi [37] to reduce the randomness of the CSI phase. However, the phase offset keeps shifting due to dynamic environmental changes, such as temperature fluctuation and the presence of obstacles.

In this paper, a novel dynamic phase calibration method is proposed to reduce the fingerprint noise and improve the accuracy of CSI fingerprint-based indoor positioning systems. A machine learning algorithm is employed to estimate the target's position. For both the offline and the online stage, the raw CSI phase of each OFDM subcarrier is extracted from a multiple-antenna wireless network using modified firmware on two access points. Then, the extracted phase information is processed with the conventional phase calibration method explained in [37]. This linear transformation method eliminates the phase errors produced on the transmitter and the receiver. To reduce phase errors from environmental changes and object movements, a dynamic phase calibration is introduced to adaptively compensate the offset by tracking the anomalous phase difference between both the CSI sample and the neighboring OFDM subcarrier. For the offline stage, the processed phase information is used to train a 1D convolutional neural network (CNN) with long short-term memory (LSTM) to establish the mapping between the fingerprint database and the corresponding position in the test site. During the online stage, the calibrated CSI phase information is processed through continuous signal measurement. The neural network estimates from the calibrated CSI phase information and provides a prediction of the target's position.

3.2 Preliminary

OFDM is commonly used in a variety of communication protocols, including the WiFi standards. In OFDM schemes, data is transmitted and received over multiple orthogonal subcarriers with different frequency spacing. A block diagram of an OFDM system consisting of a transmitter and a receiver is shown in Fig. 3.1. At the transmitter, input data is modulated and mapped to multiple subcarriers. The inverse fast Fourier transform (IFFT) is performed on each subcarrier, and a cyclic prefix is added to the digital data. Data is then converted by a digital-to-analog converter (DAC) and up-converted to the carrier frequency. At the receiver, the inverse process is performed to recover the data. Before the signal demodulation, the equalization process is conducted to compensate for amplitude attenuation and phase error. During this process, the instantaneous CSI is measured by the receiver. Therefore, CSI measurements are available for extraction without any computational overhead. At the subcarrier level, the CSI provides fine-grained information about channel conditions such as scattering, fading, and delay parameters.

A WiFi channel can be described in a flat fading model, which is

$$\boldsymbol{y} = H\boldsymbol{x} + \boldsymbol{n}, \tag{3.1}$$

where $\boldsymbol{y}$, $\boldsymbol{x}$ and $\boldsymbol{n}$ represent the received signal vector, the transmitted signal vector, and the additive white Gaussian noise (AWGN) vector, respectively. In a MIMO-OFDM system, $H \in \mathbb{C}^{M \times N \times K}$ denotes the channel matrix, where M and N are the numbers of transmitter and receiver antennas, and K is the total number of subcarriers. H represents

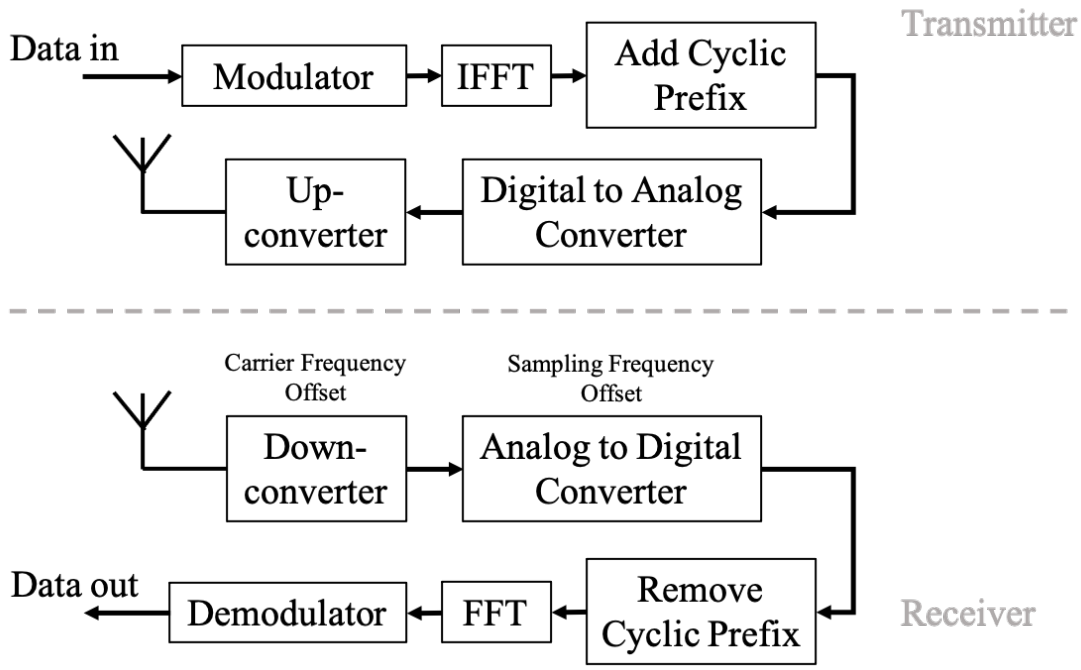

Figure 3.1: Block diagram of an OFDM transmitter and receiver.

the CSI over K subcarriers that is given as

$$H = [H_1, H_2, \ldots, H_K]^T. \tag{3.2}$$

For $M \times N$ MIMO antenna streams, let $\boldsymbol{H_k}$ defines the CSI matrix of the k-th subcarrier. It can be written as

$$H_k = \begin{bmatrix} h_{11} & h_{12} & \cdots & h_{1n} \\ h_{21} & h_{22} & \cdots & h_{2n} \\ \cdots & \cdots & \cdots & \cdots \\ h_{m1} & h_{m2} & \cdots & h_{MN} \end{bmatrix}, \tag{3.3}$$

where h_{mn} is a complex number representing the CSI of the m-th transmitter and the n-th receiver antenna stream. h_{mn} is defined as $h_{mn} = |h_{mn}| \exp(j\angle h_{mn})$, where $|h_{mn}|$ and $\angle h_{mn}$ are the amplitude and phase.

3.3 System configuration

In this section, we describe the architecture and the phase calibration process of the proposed system.

3.3.1 System Architecture

The architecture of the proposed system is depicted in Fig. 3.2. As seen, the CSI is extracted with the commodity WiFi devices. Two TL-WR2543 access points manufactured by TP-Link are used as the transmitter and the receiver.

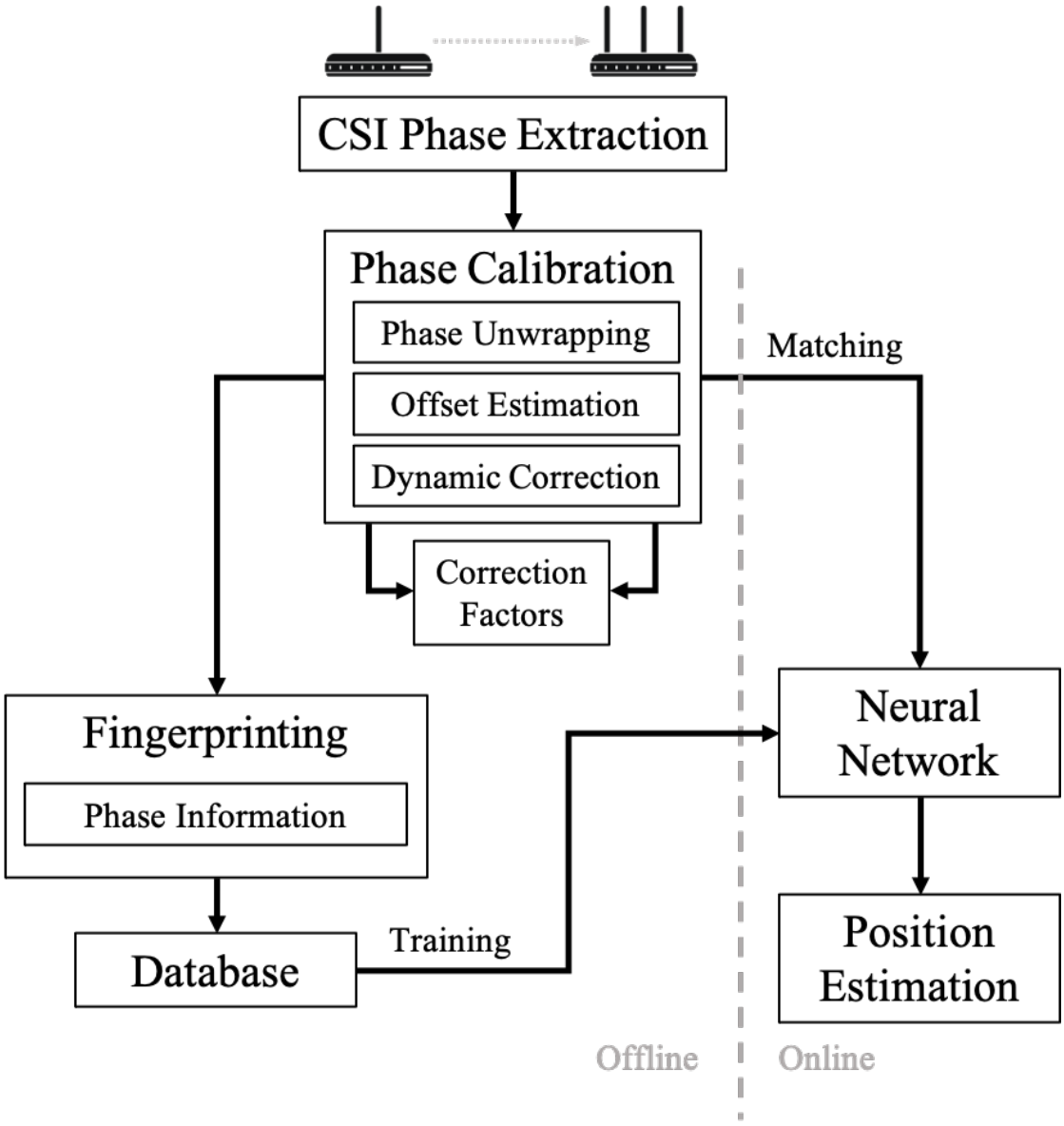

Figure 3.2: Architecture of the proposed system.

Each access point has a built-in Atheros network interface card (NIC). The access point can obtain the CSI with modified OpenWrt firmware released by the Atheros CSI Tool [38]. Both access points are remotely controlled to process the data. The system is configured as a 1×3 MIMO, with one transmitter and three receiver antennas.

In IEEE 802.11 WiFi protocol, there are 56 subcarriers for the 20 MHz bandwidth and 114 subcarriers for the 40 MHz bandwidth channel, respectively. With the help of the CSI toolkit, the Atheros NIC reports CSI from 56 available subcarriers in a 20 MHz channel [38]. The obtained CSI is represented as $H \in \mathbb{C}^{1\times3\times56}$. In total, 168 CSI data points are collected from one received packet. Unlike RSSI, which only reports one averaged value of each packet, CSI represents the channel response of each subcarrier, which significantly improves the fine granularity of the data samples.

To use the phase information as the fingerprint, the phase pre-processing is conducted on both offline and online stages for the deep learning process. Phase pre-processing includes phase extraction and calibration. The steps of phase calibration comprise phase unwrapping, phase offset estimation, and phase dynamic correction, which are explained in the next section. The fingerprint features are obtained from the processed CSI phase information and stored to train the neural network. In the neural network, the mapping is established between the fingerprint database and the target location. During the online stage, the real-time measurement of the CSI phase is calibrated and used as the input to estimate the target's position from the neural network.

3.3.2 CSI Phase Calibration and Feature Extraction

The purpose of the phase calibration procedure is to obtain a more reliable CSI phase and reduce the fingerprint noise caused by the hardware and environmental fluctuation.

The CSI phase measured by the NIC is wrapped, within the range of $[-\pi, \pi]$, which differs from the true phase by an integral multiple of 2π. The first step of phase calibration is to unwrap the measured phase to restore the appropriate multiples of 2π. At the moment of ε, for the k-th subcarrier, let $\Delta\varphi_{\varepsilon,k} = \varphi_{\varepsilon,k+1} - \varphi_{\varepsilon,k}$ represents the difference between each of two neighboring subcarriers. The unwrapped phase $\theta_{\varepsilon,k+1}$ is calculated through the following process:

$$\theta_{\varepsilon,k+1} = \begin{cases} \varphi_{\varepsilon,k+1} - 2\pi, & \Delta\varphi_{\varepsilon,k} > \pi \\ \varphi_{\varepsilon,k+1} + 2\pi, & \Delta\varphi_{\varepsilon,k} < -\pi \\ \varphi_{\varepsilon,k+1}, & -\pi < \Delta\varphi_{\varepsilon,k} < \pi \end{cases} . \tag{3.4}$$

There are two primary sources of the phase errors from the hardware of a typical OFDM system (Fig. 3.1). One is the carrier frequency offset (CFO) generated during the down-conversion at the receiver. Errors can arise during this process when the central frequencies between the transmitter and the receiver are not matched accurately due to non-synchronized local oscillations. The CFO introduces phase errors for all measured subcarriers, regardless of their subcarrier index. Another source of phase error is the sampling frequency offset (SFO) generated by the analog-to-digital converter (ADC). The SFO introduces a time delay, causing the CSI phase errors, which are proportional to the subcarrier index. Thus, the raw CSI phase information has limited usefulness as the fingerprint. The raw CSI must be calibrated before fingerprint information can be extracted.

The measured CSI phase $\theta_{\varepsilon,k}$ of the k-th subcarrier at ε moment can be expressed as

$$\theta_{\varepsilon,k} = \phi_{\varepsilon,k} + 2\pi\frac{I_k}{N}\tau_\varepsilon + \beta_\varepsilon, \tag{3.5}$$

where $\phi_{\varepsilon,k}$ represents the estimated CSI phase of k-th subcarrier at ε moment, I_k is the subcarrier index, N is the fast Fourier transform (FFT) size, τ_ε denotes a time delay caused by SFO, and β_ε is an unknown phase offset from CFO.

The total number of OFDM subcarriers for the 20 MHz WiFi channel is $K = 56$. To find $\phi_{\varepsilon,k}$ via conventional phase calibration, let a and b be the linear transformation coefficients that satisfy the following condition.

$$\arg \min_{a,b} \sum_{k=1}^{K} \left(\theta_{\varepsilon,k} - aI_k - b\right)^2. \tag{3.6}$$

Because the OFDM subcarrier is symmetric, in a simplified derivation [37], those coefficients can be defined as

$$\begin{aligned} a &= \frac{\theta_{\varepsilon,K} - \theta_{\varepsilon,1}}{I_K - I_1}, \\ b &= \frac{1}{K} \sum_{k=1}^{K} \theta_{\varepsilon,k}. \end{aligned} \tag{3.7}$$

Fig. 3.3 shows a set of raw phases from 100 CSI measurements in blue squares and the calibrated phase using the conventional linear transformation method in red dots. This phase calibrated method is stable in a static environment. However, the phase changes drastically in a dynamic environment with object movements. For example, in a 2.4 GHz WiFi band, the phase cycles through a distance of its wavelength of 0.125 m. The phase rotates when the object moves farther than the wavelength distance within a short period. According to (4), during the phase unwrapping process, if the criteria $|\Delta\varphi_{\varepsilon,k}| > \pi$ or $|\Delta\varphi_{\varepsilon,k}| < \pi$ is altered by the phase rotation, an error of $|2\pi|$ will be introduced. The phase difference can be used to overcome this problem. In the OFDM scheme, the frequency spacing of other subcarriers is evenly distributed. With respect to

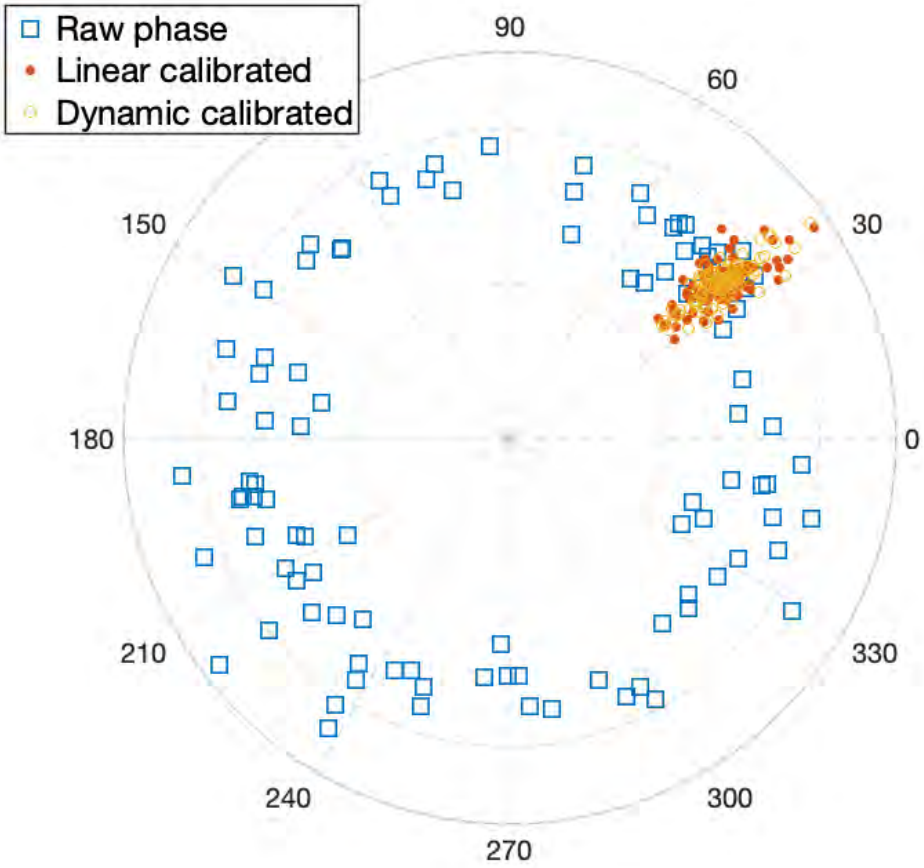

Figure 3.3: Raw phase (blue) of 100 CSI measurements, same data after linear calibration (red), and after dynamic calibration (yellow).

the first subcarrier, the equivalent wavelength among those subcarriers becomes much longer, which reduces the sensitivity to the object movement in a static environment.

Two metrics are defined: for the k-th subcarrier, 1) the phase difference between neighboring subcarriers $\Delta\xi_k$, and 2) the phase difference between adjacent CSI samples $\Delta\psi_k$,

$$\begin{aligned} \Delta\xi_k &= \phi_{\varepsilon,k+1} - \phi_{\varepsilon,k}, \\ \Delta\psi_k &= \phi_{\varepsilon+\Delta t,k} - \phi_{\varepsilon,k}, \end{aligned} \tag{3.8}$$

where ε is the sampling time, and Δt is the sampling interval. In our configuration, the total number of subcarriers is $K = 56$. so the sets of those phase differences are $\Xi_\varepsilon = \{\Delta\xi_1, \Delta\xi_2, \cdots, \Delta\xi_{K-1}\}$ and $\Psi_\varepsilon = \{\Delta\psi_1, \Delta\psi_2, \cdots, \Delta\psi_K\}$.

To identity any error of $|2\pi|$ occurred during phase unwrapping, $\Delta\xi_k$ is smoothed by the following condition:

$$\Delta\xi_k = \begin{cases} \Delta\xi_k, & |\Delta\xi_k| < \sigma|\max(\Xi)| \\ \Delta\xi'_k, & \text{otherwise} \end{cases}, \tag{3.9}$$

where $\Delta\xi'_k = avg(\Xi) + (1-\delta)\Delta\xi_k$, δ is the correction factor, and σ defines a threshold of the maximum value. Then, the smoothed $\Delta\xi_k$ is then added back to restore the calibrated phase $\phi_{\varepsilon,k+1}$.

The received data samples are in a sequence of transmitted packets. In consonance

with (5) and (8), the phase difference between measured CSI samples is described as

$$\begin{aligned}\Delta\theta_k &= \theta_{\varepsilon+\Delta t,k} - \theta_{\varepsilon,k} \\ &= (\phi_{\varepsilon+\Delta t,k} - \phi_{\varepsilon,k}) + 2\pi\frac{I_k}{N}(\tau_{\varepsilon+\Delta t} - \tau_\varepsilon) \\ &\quad + (\beta_{\varepsilon+\Delta t} - \beta_\varepsilon) \\ &= \Delta\psi_k + 2\pi\frac{I_k}{N}\Delta\tau_k + \Delta\beta_k,\end{aligned} \tag{3.10}$$

which holds the corresponding phase difference of all the subcarriers between the previous and current packets with Δt interval. In the ideal case, at the packet transmitting interval of a few hundredths of a second, the variation of $\Delta\tau_j$ and $\Delta\beta_j$ are minimal, while the phase from the adjacent CSI sample follows a relatively similar trend. Thus, $\Delta\psi_k$ fits within a small number of phase differences. However, the environment can have a severe impact from one moment to another, which causes phase errors during unwrapping. To mitigate the impact of uncertain phase rotation in equation (10), the slope and intercept point (a', b') can be solved by satisfying this condition:

$$\arg\min_{a',b'} \sum_{k=1}^{K} \left(\Delta\theta_k - a' I_k - b'\right)^2. \tag{3.11}$$

After linear transformation, the slope a' indicates the variation of $\Delta\psi_k$. Define a confident interval η for slope a', when a' out of the range of η, the measured phase $\theta_{\varepsilon+1,k}$ that contains the corresponding $\Delta\psi_k$ is discarded.

Once each measured CSI phase has been updated by the aforementioned phase correction process, a and b can be derived from (6).An example of dynamic phase calibration results is shown in Fig. 3.3 as the yellow circles. Depends on the testing environment, the value of δ and η are optimized and maintained in a database as part of the fingerprint.

The adaptively calibrated phase information is stored in the database for neural network training.

3.3.3 Neural Network Model

The neural network includes the input layer, the 1-D convolutional neural network (CNN) layers, the long short-term memory (LSTM) layers, the fully connected linear layer, and the output layer. They are $X \times Y$ positions corresponding to the location grid on the floor, where X and Y are the numbers of grids on the horizontal and vertical axis. The input is a matrix $\phi_\varepsilon \in \mathbb{C}^{M \times N \times K}$ that consist of the CSI phase information, where M and N are the numbers of transmitter and receiver antennas, and K is the number of subcarriers. The convolutional layer acts as a low-level feature extractor, which is applied to reduce the data size and computational complexity. After the convolutional layer, the LSTM and linear layers are used for better network expressiveness of the sequential data.

The neural network is trained by phase information that is labeled with grid index, and using stochastic gradient descent with the negative log likelihood (NLL) loss function shown in (12).

$$\text{Loss} = -\sum_{i=0}^{P}\sum_{j=0}^{Q} t_{i,j} \ln\left(T_{i,j}\right), \tag{3.12}$$

where P is the batch size of the stochastic gradient descent and Q is the number of classifiers. $t_{i,j}$ and $T_{i,j}$ are the ground truth vector and predicted vector of the probability distribution. The number of epochs impacts the performance of the network model, respectively. An epoch is selected from the best validation results before overfitting occurs. The system predicts the result by finding the class with the greatest softmax output.

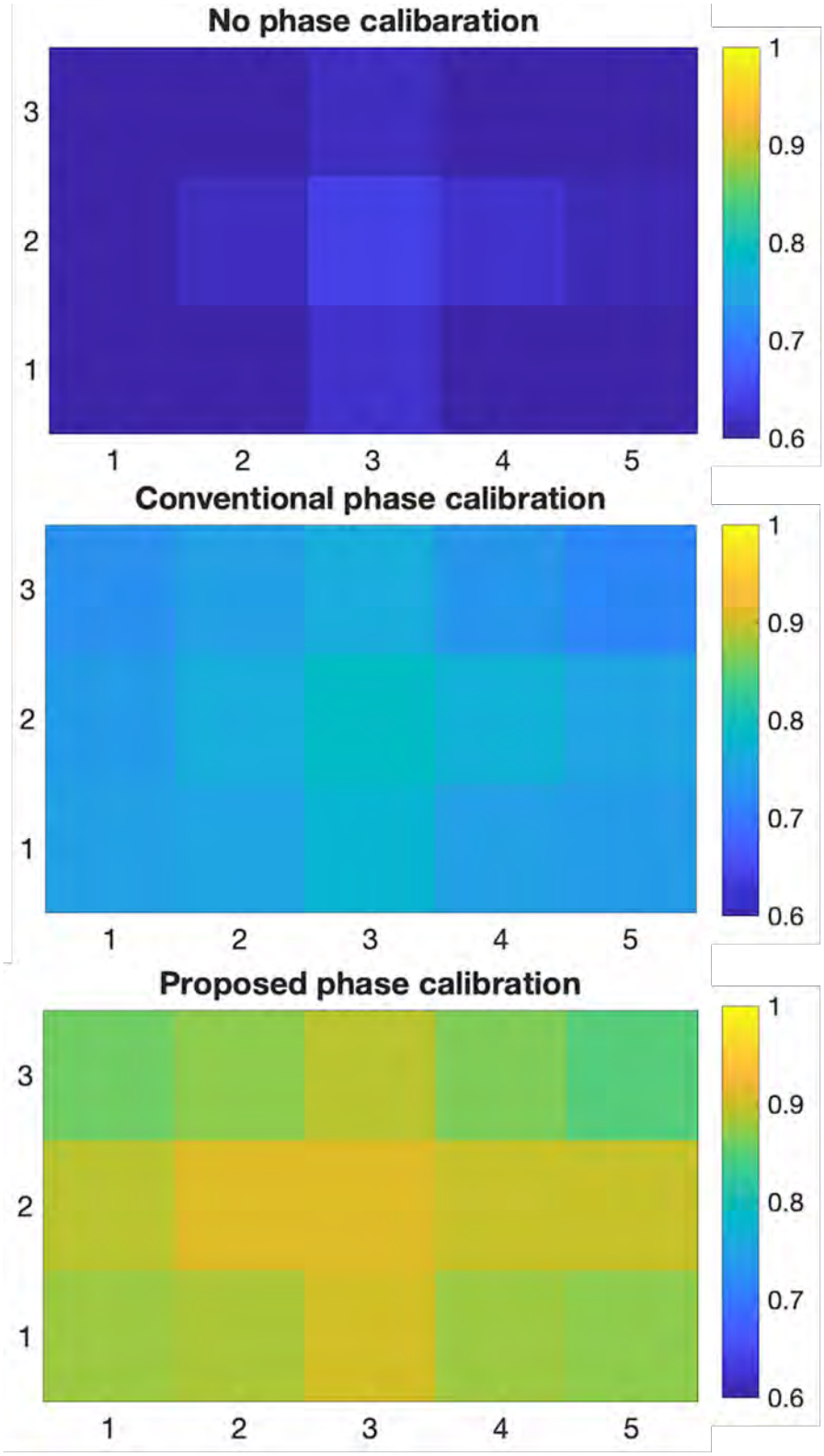

Figure 3.5: MoE prediction rate per grid by different phase dataset: (a) dataset # 1: Unwrapped raw phase. (b) dataset # 2: Conventionally calibrated phase (c) dataset # 3: Dynamically calibrated phase.

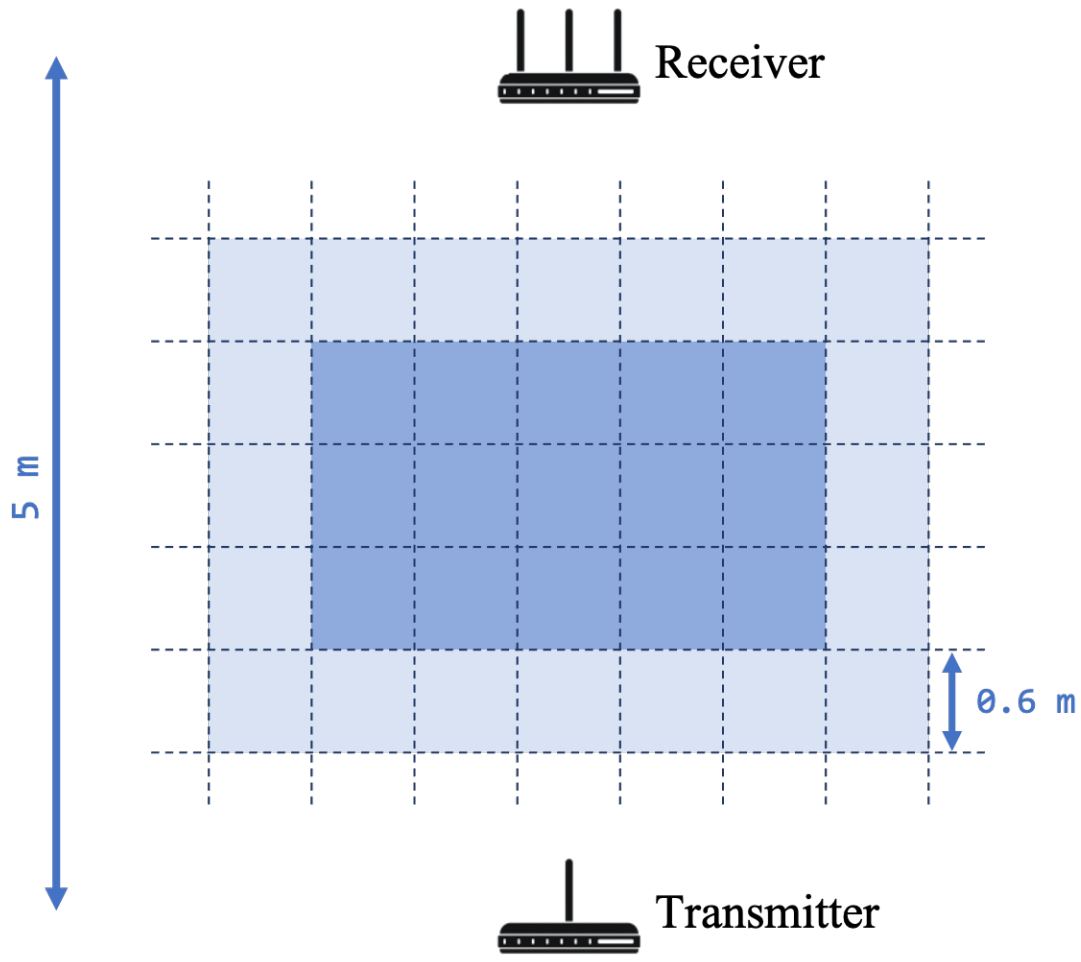

Figure 3.4: Testsite topology: transmitter, receiver, and floor grid placement.

Table 3.1: Prediction rate and position error across datasets.

	Data #1	Data #2	Data #3
Predicted rate (%)	60.1	75.2	88.4
Averaged error (m)	2.35	1.69	1.33

3.4 Experiments

Fig. 3.4 shows the setup of the experiment system. The testing field is a 7 m $\times$ 6 m area with the grids marked on the floor. Each grid is approximately 0.6 m $\times$ 0.6 m. A total of 15 grids (rendered as a darker blue area in Fig. 3.4) in the central area comprise the core testing site to evaluate the system performance. The light blue areas are secondary areas for analyzing positioning errors.

The transmitter and receiver are placed on the short sides of the testing field. They are set 5 m apart and directly facing each other. The transmitter and receiver are mounted on a platform that is 1.2 m above the floor. A person moves among the center of each grid to gather the data at each location. Position performance is analyzed by the successful prediction rates and failure prediction rates with a margin of error (MoE) model. The MoE model considers any predicted grid that lands on a surrounding grid as a successful prediction. Grids that are close to the ground truth are more likely to be predicted as being occupied. Even without a defined explicit distance metric in the loss function, the network model learns features relevant to the regions of interest. The results include both successful prediction and failure prediction are adopted to evaluate positioning accuracy. The position error is calculated by averaging the distance between the predicted grid and the actual grid, regardless of the MoE model.

The system is evaluated from three different sets of fingerprints: the unwrapped raw phase, the conventional linear fitted phase, and the dynamically calibrated phase. The heat map shown in Fig. 3.5 suggests that the proposed phase calibration method has a

higher overall success rate than the conventional linear calibration and non-calibration methods. Within the test site, the successful prediction rate is highest in the central area and gradually degrades to the corners. Table I compares the overall prediction rates and average position errors across three datasets. The dynamic calibrated CSI phase reaches an 88.4% successful rate, while the prediction rates of the unwrapped raw CSI phase and the linear calibrated phase are 60.1% and 75.2%, respectively. The average position errors of those three datasets are 2.35 m, 1.69 m, and 1.33 m. Comparing to the conventional linear transformation method, the proposed phase calibration method improves the prediction rate by 13.2% and reduces the average position error from 1.69 m to 1.33 m by 21.3% .

3.5 Conclusions

In this paper, two commodity wireless access points with built-in Atheros NIC were utilized for CSI phase extraction. A novel phase calibration method was proposed, which introduced two phase correction factors to improve the phase calibration process dynamically. A multi-layer neural network was trained to estimate the target's position. The results where evaluate both the prediction rate in an MoE model and the average position error illustrated that the use of the conventional linear transformation calibration method was suffered from a drop in prediction rate and, therefore, a lower position accuracy. For the CSI-based positioning system, the proposed method outperformed the conventional linear transformation calibration method by 13.2% higher prediction rate and reduces the average position error 21.3%.

WiFi-based Environment Adaptive Positioning with Transferable Fingerprint Features

Guangxin Wang, Arash Abbasi, and Huaping Liu

IEEE 11th Annual Computing and Communication Workshop and Conference (CCWC)

Artificial Intelligence and Machine Learning

Las Vegas, NV

27-30, January 2021

Chapter 4: WiFi-based Environment Adaptive Positioning with Transferable Fingerprint Features

Abstract: Channel state information (CSI)-based fingerprint approach for WiFi-based indoor localization has attracted a lot of attention recently. The fine-grained CSI represents the location-dependent channel characteristics more effectively than the coarse-grained received signal strength indicator (RSSI). However, the CSI fingerprints can deviate drastically with environmental variations. Consequently, the CSI-based fingerprint positioning models need to be adapted for different environments and/or updated over time, which is time-consuming and labor-intensive in practice. In this paper, an environment-adaptive positioning system is proposed to transfer the fingerprint features that significantly reduce reconstructing the fingerprint database. A CSI extraction platform is developed based on the modified OpenWrt firmware, enabling access to CSI measurements on commodity WiFi devices. To transfer the fingerprint features, a domain adaptation approach is proposed to reconstruct the CSI fingerprint database from the existing fingerprints with a limited number of new measurements. Experiments are conducted in several real-world test sites, including the laboratory and the lounge, with environmental change. The results show that the performance of the proposed system is promising in terms of localization accuracy and adaptation efficiency.

4.1 Introduction

With the rapid development of mobile devices and smart applications, location-based services (LBS) have become essential in many fields, including route guidance, geolocation social media, and mobile advertising. Because a lot of the mobile devices are operated in indoor environments, many LBSs need indoor positioning solutions [20, 24, 25] to acquire the object location, which has created extensive research interest. Most indoor positioning solutions are based on radio frequency (RF) signals that are enabled by either dedicated tags like Bluetooth and radio-frequency identification (RFID), WiFi infrastructure [39] or transmitters such as ultra-wideband (UWB) [40, 41]. In both cases, fingerprint-based approaches play an important role in indoor positioning systems [42][26]. Such systems do not require the physical attachment of any device on the object. The basic principle of the fingerprint approach is to find an object location by comparing the signal pattern between the transmitter and receiver to a pre-defined fingerprint database of that pattern. Generally, the fingerprints used to represent the signal pattern are received signal strength indicator (RSSI) and channel state information (CSI). Most of the proposed indoor positioning fingerprinting approaches use WiFi as their RF signal source because WiFi is widely available in buildings and enabled on most smart devices. Moreover, the WiFi-based systems can be deployed without the installation of any other dedicated infrastructures. In some approaches, RSSI is commonly used as the fingerprint due to its simple nature [26] [27]. However, RSSI measures the average amplitude of the received data and, therefore, only provides coarse-grained channel information. In contrast, the CSI contains both amplitude and phase information measured on each orthogonal frequency-division multiplexing (OFDM) subcarrier. In previous studies, access to fine-grained CSI has been enabled through the use of modified firmware on

commodity WiFi hardware[29, 43, 44]. For CSI, the finer granularity and less sensitivity to background noise and environmental changes make it a better choice for fingerprint features. Researchers have increasingly focused their attention on CSI rather than RSSI when developing WiFi-based fingerprinting systems [4].

One of the significant challenges of CSI-based systems is improving their robustness against environmental changes. Many applications have been developed using CSI, but they have not considered the impact of environmental changes [45] [46]. The CSI describes the signal propagation through multipath channels between the transmitter and receiver. Due to reflection, diffraction, or scattering, environmental variations change the multipath dynamic and lead to a biased distribution of the CSI fingerprint. Any change in the environment, such as object movement or a rearranged setup, can cause a drastic deviation of the real-time CSI measurements from the previously collected fingerprint, resulting in a performance drop. The fingerprint database generated at a particular time in one area cannot serve as a useful reference for consistent positioning in long-term deployments or other test fields. This lack of robustness tends to degrade the reliability of such systems, especially CSI-based systems dependent on machine learning algorithms to exploit the fingerprint database [47–49]. In these cases, the database reconstruction of the whole area is required, which is time-consuming and labor-intensive. In practice, it becomes infeasible to rebuild the database and retrain the neural networks for the entire region of interest over different times.

In this paper, a domain adaptation method is proposed, which generalizes the use of CSI fingerprinting to work adaptively in dynamic environments. The WiFi-based positioning system consists of the positioning models and the transfer learning models with the adaptive neural network. A CSI-enabled platform is developed to access the CSI directly from the commodity WiFi devices, rather than using the computer as a

receiver for CSI extraction. In the hardware, the non-synchronized local oscillations between the transmitter and receiver, as well as sampling frequency shift during analog-to-digital conversion, result in time-variant random phase offsets of the CSI. To overcome this problem, a phase calibration scheme is adopted to sanitize the raw CSI data. The sanitized CSI data preserves the position-related characteristics while removing the phase offset from the hardware imperfections. Instead of CSI phases, the CSI phase differences across each subcarrier are utilized to generate the fingerprint database. The positioning model includes a neural network and an adaptation model. A discrepancy exists in the position feature distribution between the source domain (training site) and the target domain (untrained site) due to environmental divergence, and the neural networks can learn transferable features for domain adaptation [50]. To transfer the fingerprint features to the target domain, the proposed system aims to map the source domain and the target domains as a common space and uses the CSI fingerprints from the source domain with a few supplementary fingerprints from the target domain to minimize the disparities between the two domains. As a result, with the help of transferring the position features from the source site, the positioning system predicts the location of the object at the target site with a limited number of fingerprint reconstructions.

The rest of the paper is organized as follows. Section II summarizes the background and related work. Section III introduces the detailed framework design of the proposed system. Section IV explains the experiment procedure and presents the results and analysis. Section V concludes the paper.

4.2 Related Work and Background

4.2.1 Related Work

Various approaches are proposed in the previous studies to address the challenges of using indoor positioning systems in a dynamic environment. Some non-learning based methods use the signal propagation metrics such as the Doppler shifts and angle of arrival (AoA) to reduce environmental impact. In [51], to find the subcarriers affected by multipath signals, multiple transceivers are used to model the channel fading profile from the CSI measurements. A probabilistic model of spatial Doppler and AoA information is proposed in [52], which obtains the Doppler velocity from CSI and combines with the AoA to track the object location. Multiple receivers are used to estimate the object trajectory, which derive Doppler velocity and AoA from the CSI measurements simultaneously [53].

Other works rely on machine learning methods to fully exploit the channel information for measurements. An environment-independent localization approach is introduced in [54], which uses the fingerprints from multiple antennas to train the model and revise the values affected by environmental variations. In [55], a neural network is employed to train a model that provides training samples for each target domain from the source domain. However, machine learning algorithms are frequently restricted by the number of data points that need to be learned. Lack of sufficient input data limits the ability to gain accurate knowledge. To mitigate this issue, transfer learning aims to gain knowledge from one problem and apply it to another related problem with only a limited number of known data.

4.2.2 Transfer Learning

In general, transfer learning contains two domains: a source domain and a target domain denoted by $\mathcal{D}^s$ and $\mathcal{D}^t$, respectively [56]. The process of transferring the information from the source domain $\mathcal{D}^s$ to the target domain $\mathcal{D}^t$ is to minimize the difference of probability distribution between the source data and target data. Dynamic environment positioning is one of the applications using transfer learning. The knowledge obtained from CSI fingerprints in one location can be used to construct a prediction model in another location. This transfer learning process is called domain adaptation, which reduces the difference of feature distribution between the source and target and lowering the risk of overfitting the model.

4.2.3 Channel State Information

Modern commodity WiFi devices with a built-in network interface card (NIC) are equipped with multiple antennas for multiple-input and multiple-output (MIMO) communication systems. The instantaneous CSI is estimated by the NIC for each OFDM subcarrier. In time domain, the channel impulse response (CIR) of WiFi is described as,

$$h(\tau) = \sum_{p=1}^{P} a_p \exp\left(j\theta_p\right) \delta\left(\tau - \tau_p\right), \tag{4.1}$$

where P indicates the total number of paths, a_p, θ_p, and τ_p represent the amplitude, phase, and propagation delay of the p^{th} path, respectively, and $\delta(\tau)$ is the Dirac delta function. In the frequency domain, the CSI of all OFDM subcarriers are calculated by

the receiver as the complex values, which can be represented as

$$h = |h| \exp(j\angle h), \tag{4.2}$$

where $|h|$ and $\angle h$ represent the amplitude and phase, respectively. Note that, a matrix of h is contained in the CSI sample $H \in \mathbb{C}^{M \times N \times S}$, where M, N, and S are the number of transmitter antennas, the number of receiver antennas, and the number of OFDM subcarriers, respectively.

4.3 System Design

4.3.1 CSI enabled Platform

Most existing CSI-based systems adopt the Intel IWL5300 NIC tool to extract the CSI data from a computer that equips with external WiFi NIC cards [43]. However, the driver of the Intel IWL5300 NIC tool kit is proprietary and does not allow modification, and the IWL5300 NIC tool only reports 30 out of 56 subcarriers for the 20MHz WiFi channel. Moreover, the external NIC limits the usage of this tool for portable and large-scale applications.

To overcome these problems, a CSI-enabled platform is developed in which the CSI measurements are directly extracted from the commodity WiFi devices. In our case, instead of the Intel IWL5300 NIC, two TP-Link access points are used, and each access point has a built-in Atheros NIC. The access points are flashed with OpenWrt firmware, which is a Linux-based open-source operating system designed for wireless routers and access points. Then, a revised version of OpenWrt is modified based on the Atheros CSI

Tool [44]. The platform reports CSI data on all the available subcarriers and therefore provides more enriched information than the IWL5300 CSI tools. For the 20 MHz WiFi channel, each transmitter and receiver antenna stream produces 56 CSI measurements.

4.3.2 Neural Networks

To apply domain adaptation, the probability distributions of the CSI fingerprints in both the source and the target domains need to be unified by mapping them into a common space. Thus, the positioning model using the CSI fingerprints for the target domain can be generated from both the source and the target domains. A neural network is built to accomplish the mapping. The input of the neural network is the CSI fingerprint database from the source and the target domains, and the output is the transferable features of the fingerprints in the common space. The goal is to minimize the divergence of the probability distributions of the mapped fingerprints between the source and the target domains. During CSI preprocessing, the CSI fingerprints are collected at each location, and a phase calibration scheme is applied to sanitize the raw CSI data. The phase offset of the CSI is calculated through a phase calibration method to remove phase errors and fingerprint noise. The preprocessed CSI fingerprints are used for both the offline training and the online testing step. For the offline training step, a fusion of one-dimensional convolutional neural network (CNN) and the long-short-term-memory (LSTM) is employed as the source positioning model that establishes the correlation between CSI fingerprints and location grids. Then, the CNN-LSTM network is trained using the CSI fingerprints labeled with the grid index of each location. During the online step, the real-time CSI measurements are preprocessed and input into the CNN-LSTM model, which predicts the object position. The source positioning model has one input

layer and one output layer, along with fully connected layers between the 1D-convolutional layer and LSTM layers.

4.3.3 Domain Adaptation Networks

The purpose of domain adaptation is to reduce the feature distribution difference between the source and target domain. The Euclidean distance is used to evaluate the distribution discrepancy of CSI fingerprints. Define $\mathcal{D}^s = (d_i^s, g_i^s)$ and $\mathcal{D}^t = \left(d_j^t, g_j^t\right)$ as the fingerprint datasets of the source domain and target domain, where d_i^s and d_j^t represent the fingerprint features of CSI, g_i^s and g_j^t represent the labels of the location grids, in which $i = 1, 2, \cdots, N_s$ and $j = 1, 2, \cdots, N_t$. The numbers of training samples of the source domain N_s and the target domain N_t satisfy this criteria $N_s \gg N_t$. The source domain fingerprint dataset $\mathcal{D}^s$ is used to train the source positioning model. The loss function L_P of the positioning model is defined as the mean distance error between the actual grid and the predicted grid as

$$\begin{aligned} L_P &= \frac{1}{N_s} \sum_{i=1}^{N_s} f_D \left(f_E \left(d_i^s \right), g_i^s \right) \\ &= \frac{1}{N_s} \sum_{i=1}^{N_s} \sqrt{\left(\hat{x}_i^s - x_i^s\right)^2 + \left(\hat{y}_i^s - y_i^s\right)^2}, \end{aligned} \tag{4.3}$$

where $f_D(\cdot, \cdot)$ represents the Euclidean distance function, $f_E(\cdot)$ is the position estimation function, (x_i^s, y_i^s) and $(\hat{x}_i^s, \hat{y}_i^s)$ are the coordinates of the actual grid and the predicted grid of the i^{th} data point, respectively.

To match the probability distributions of CSI fingerprints between the source and the target domains, a domain adaptation model is proposed to map the CSI fingerprints. The

Euclidean distance is utilized to evaluate the training process of the domain adaptation model. The object is to map the CSI fingerprints of the probability distributions between the source domain and the target domain with minimized Euclidean distance. To train the adaptive model, a small portion of data samples are randomly selected from both the source and the target training datasets. Assume the number of selected location grids is M, and the number of the fingerprint data points from each grid is N, the loss function L_D of the domain adaptation model is defined as

$$L_D = \frac{1}{MN} \sum_{m=1}^{M} \sum_{n=1}^{N} f_D \left(f_M \left(d_{m,n}^s \right), f_M \left(d_{m,n}^t \right) \right), \tag{4.4}$$

where $f_M(\cdot)$ is the mapping function of the domain adaptation model, $d_{m,n}^s$ and $d_{m,n}^t$ are the n^{th} fingerprint of the m^{th} location picked from the source and the target training dataset. The domain adaptation network contains a combination of the source positioning model and the domain adaptation model.

When the input is the dataset from the source domain, the adaptive network estimates the object position and behaves as the positioning model $f_E(\cdot)$ that is trained to minimize the localization loss L_P as described in (3). Otherwise, when using the selected data from both the source and the target domains, instead of exporting the estimated position, the adaptive network serves as the domain adaptation model $f_M(\cdot)$ to minimize the domain loss L_D expressed in (4). By connecting the positioning and domain adaptation, the objective is to train both models as one system that minimizes both the localization loss L_P and the domain loss L_D. The domain adaptation network is established when the

total loss L reaches its minimal, where

$$L = L_P + L_D = \frac{1}{N_s}\sum_{i=1}^{N_s} f_D\left(f_E\left(d_i^s\right), g_i^s\right) + \frac{1}{MN}\sum_{m=1}^{M}\sum_{n=1}^{N} f_D\left(f_M\left(d_{m,n}^s\right), f_M\left(d_{m,n}^t\right)\right). \tag{4.5}$$

To validate whether the CSI fingerprint fits the current domain, a domain discriminator is designed using a similarity checking model. The presence of a significant mismatch in the discriminator indicates a significant event of environmental change. When those events occur, a new target domain is created, and additional training data are requested from the target domain to conduct the adaptation process.

4.4 Experiment and Evaluation

4.4.1 System Setup

The hardware setup consists of two TP-Link TL-WR2543 wireless routers, which are set as access points. Each of the access points is equipped with an Atheros AR9380 NIC that is compatible with the modified OpenWrt firmware. One access point operates as the transmitter with one transmitter antenna. Another access point, with three receiver antennas, operates as the receiver to extract the real-time CSI measurements. A laptop connected to both access points controls the transmitted data sequence on the transmitter and retrieves the recorded CSI from the receiver. Both NICs are configured to operate on a 2.4 GHz WiFi channel with 20 MHz bandwidth. The packet transmitting rate is set at 100 packet/second. The sampling rate on the receiver is set accordingly. In the case of a packet loss, the CSI is padded with interpolation to ensure stable CSI data

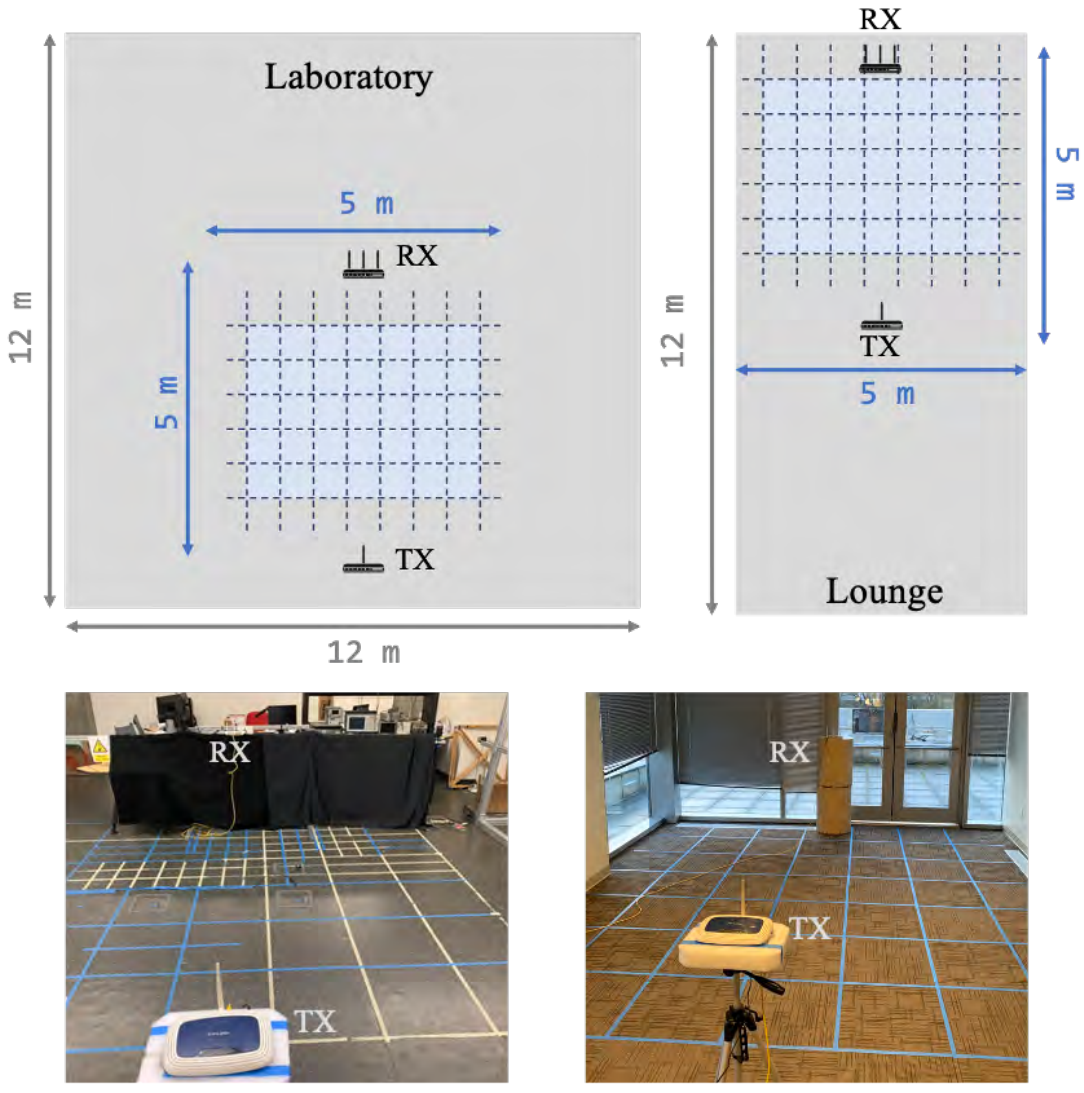

Figure 4.1: Topology of the test site: the laboratory (left) and the lounge (right).

for fingerprint feature extraction. The gathered CSI data are transferred to another computer for backend processing, which has an Intel Core i7-9700k CPU with 16 GB RAM and a discrete Nvidia RTX GPU.

As shown in Fig. 4.1, the experiments are conducted in two different rooms, a laboratory ($10m \times 10m$) and a lounge ($12m \times 5m$). The laboratory has metal cabinets and other testing equipment, and the lounge has few pieces of furniture. A $5m \times 5m$ test site is located in each room. Each test site has grids marked on the floor, and each grid is about $0.6m \times 0.6m$. The transmitter and receiver are placed $5m$ apart and directly facing each other. In each room, the CSI is measured when a person stands at the center of each grid. Extra datasets are captured during different times of the day to validate the environment dynamics. Additional datasets are gathered to recalibrate the database when the discriminator indicates significant environmental changes.

4.4.2 Performance within Same Room

The system performance is evaluated by execution time, including the initial training time and the adaptation training time. The initial training time consists of the training data collection time and the positioning model training time. The adaptation time includes the time it takes to collect recalibration data, and the time it takes to train the adaptation model. The execution times for both test sites are shown in Table I. Because both test sites have a similar size and room setup, these execution times are very close during both the initializing and recalibration processes. The positioning performance is calculated based on the successful prediction rates for each location. In addition to the direct match, a margin of error (MoE) model is applied, which considers any predicted position that lands on a surrounding grid as a successful prediction. As shown in Table

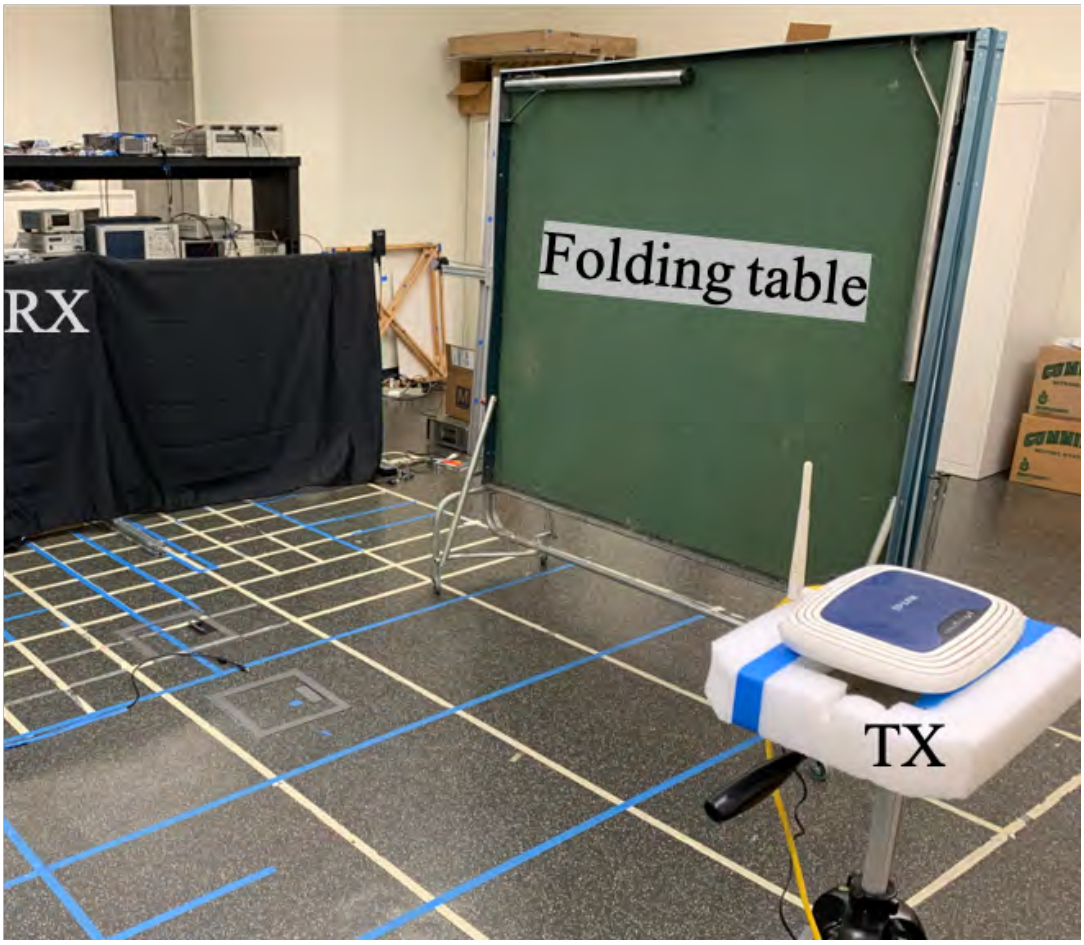

Figure 4.2: Obstacle present at the test site of the laboratory.

Table 4.1: Predicted rate and averaged error within the same room.

	Lab	Lab (w/ table)	Lounge
Predicted rate (%)	84.3	77.2	91.7
Averaged error (m)	1.51	1.77	1.26

Table 4.2: Predicted rate and averaged error across two rooms.

	Lounge to Lab	Lab to Lounge
Predicted rate (%)	60.2	63.5
Averaged error (m)	2.37	2.16

4.1, the average prediction rates for the laboratory and lounge are 84.3% and 91.7%, and the averaged errors are $1.51m$ and $1.26m$, respectively. In the lounge, the decreased number of furniture and equipment causes fewer multipath reflections, which relates to a 7.4% positioning prediction increase.

Additionally, to evaluate the system performance with room setup changes, a folding table as an obstacle with the height of $1.8m$ and the width of $1.5m$, is placed at the side of the test site in the laboratory (Fig. 4.2). The domain discriminator does not consider this change as a new target domain and does not request recalibration data. The positioning estimation is completed with a successful prediction rate of 77.2%. The presence of the obstacle in the laboratory decreases the prediction rate by 7.1%, and the averaged estimation error drops from $1.51m$ to $1.77m$.

Table 4.3: Execution time of both training and adaptation process.

	Training Time (s)		Adaptation Time (s)	
	Collection	Modeling	Collection	Modeling
Lab	5070	1100	1360	1900
Lounge	4850	1050	1270	1880

4.4.3 Performance across Two Rooms

In this part of the experiment, the system performance is evaluated across two rooms. First, the data from the lounge is selected as the source domain for training and uses the laboratory as the target. The position estimation is conducted at the laboratory. Then, the roles of the lounge and laboratory are switched for the source domain and target domain, and the same procedure is done in the lounge. To accommodate the environmental dynamics from one room to another, domain adaptation is performed to save time and labor. The transferable features from the fingerprint database are adopted from one room and applied to another. For both scenarios, the domain discriminator detects a new target domain, and additional data are fulfilled.

As shown in Table 4.2, the successful prediction rates for these two scenarios are 60.2% and 63.5%, and the averaged errors are $2.37m$ and $2.16m$, respectively. Comparing the system performance degradation between Table 4.1 and Table 4.2, adapting the fingerprint features from the lounge to the laboratory brings a 24.1% predicted rate drop, and it is 28.2% when adapting the fingerprint features from the laboratory to the lounge. The 4.1% difference indicates that the fingerprints of the lounge contain more transferable features than the laboratory.

As shown in Table 4.3, the initialization of gathering a new set of fingerprints through data collection and training is extremely time-consuming and labor-intensive. In the laboratory, compared to the initialization data collection (5070 seconds) and training time (1100 seconds), the recalibration process of the adaptation uses a total of 3260 seconds, which is 52.8% of the initial execution time. Similarly, it saves 46.7% of the execution time in the lounge. For the recalibration process, the time difference between the conventional and adaptive method is 2750 seconds.

4.5 Conclusions

In this paper, a novel domain adaptation scheme was proposed to estimate the position of an object in different environments. A WiFi-based platform was developed to access the real-time CSI through specialized OpenWrt firmware. A neural network model was designed for positioning and domain adaptation purposes. The model was trained by labeled CSI fingerprints from the source domain. Then, the transferable features of the CSI fingerprint between the source and the target domains are mapped into a common space during the domain adaptation process. A discriminator was utilized to detect the environmental changes and request a supplemental training set to recalibrate the adaptation process. The results showed the system adapted to environmental changes within the same test site when a large obstacle was blocking the area. Although it came at the cost of a lower predicted rate and positioning accuracy, with additional adaptation data, the system was able to transfer the feature knowledge from one room to another.

Impacts of High dose 3.5 GHz Cellphone Radio Frequency on Zebrafish Embryonic Development

Subham Dasgupta, Guangxin Wang, Michael T. Simonich, Tingwei Zhang, Lisa Truong, Huaping Liu, and Robyn L. Tanguay

PLOS One

vol. 15, no. 7, 2020

Chapter 5: Impacts of High dose 3.5 GHz Cellphone Radio Frequency on Zebrafish Embryonic Development

Abstract: The rapid deployment of 5G spectrum by the telecommunication industry is intended to promote better connectivity and data integration among various industries. However, since exposures to radio frequency radiations (RFR) greater than 2.4 GHz are still uncommon, concerns about their potential health impacts are ongoing. In this study, we used the embryonic zebrafish model to assess the impacts of a 3.5 GHz RFR on biology - a frequency typically used by 5G-enabled cell phones and lies within the 4G and 5G bandwidth. We established a plate-based exposure setup for RFRs, exposed developing zebrafish to 3.5 GHz RFR, specific absorption rate (SAR) $\approx$ 8.27 W/Kg from 6 h post fertilization (hpf) to 48 hpf, and measured a battery of morphological and behavioral endpoints at 120 hpf. Our results revealed no significant impacts on mortality, morphology or photomotor response and a modest inhibition of startle response suggesting some levels of sensorimotor disruptions. This suggests that the cell phone radiations at low GHz-level frequencies are likely benign, with subtle sensorimotor effects. Through this assessment, we have established a robust setup for zebrafish RFR exposures readily amenable to testing various powers and frequencies. Future developmental exposure studies in zebrafish will evaluate a wider portion of the radio frequency spectrum to discover the bioactive regions, the potential molecular targets of RFR and the potential long-term effects on adult behavior.

5.1 Introduction

The advancement of wireless communication technologies over the past decade provides faster connectivity and more bandwidth to a wider population integrating commerce, education, healthcare and consumer applications through interconnected devices. A recent step forward is the 5th generation or 5G wireless technology, currently under a gradual coverage schedule limited by the rate at which necessary infrastructure upgrades can be deployed. The 5G spectrum will cover radio frequencies from < 1 GHz to microwave frequencies up 300 GHz; part of these frequencies (< 5 GHz) overlap with existing 4G LTE and WiFi spectrums. Low band spectrums (< 1 GHz) will enable connection to remote areas, whereas mid-band (1–6 GHz) and the spectrum range (> 24 GHz) will ensure better and wider connectivity to individual devices as well as device-to-device connectivity through the Internet of Things (IoT) [57, 58]. As we move to higher spectrum ranges transmitted among our devices, the potential for health effects from higher radio frequency radiation (RFR) should be examined.

Although no part of the radio or microwave range constitutes ionizing radiation, several studies have associated RFR exposures with adverse health effects such as neuropsychiatric problems, carcinogenicity, neurodegenerative diseases, genotoxicity, lowered sperm quality and impacts on the circulatory, immune, endocrine and skeletal systems [59–62]. Some of these effects are almost certainly thermal in origin, resulting from tissue absorption of higher energy photons with increasing frequency [61, 63]. Thermal effects are readily sensed and easily mitigated, and the ability of RFR to penetrate tissue declines linearly with increasing frequency [64]. Despite many efforts, RFR impacts on biology by non-thermal mechanism(s) remain poorly established, but not yet discountable either.

The impact of RFR on developmental health, in particular, needs better assessment.

Developmental stages are the most sensitive to external stressors because the full repertoire of biological targets and molecular processes are operational during organogenesis. Embryonic development thus represents the ideal biological window to determine whether external stressors can interact with and perturb biological functions. Subtle adverse effects on development can also have long term consequences. Recently, the National Toxicology Program conducted a chronic 2-year study on the effects of relatively high dose RFR on carcinogenesis in rats (900 MHz exposure; up to a specific absorption rate (SAR) of 6 W/kg and mice (1900 MHz exposure; up to SAR of 10 W/kg), with RFR exposures beginning in utero during the prenatal phase of the test animals. For comparison, the basic limits for human whole-body exposure in terms of SAR are 0.4 W/kg in occupational settings and 0.08 W/kg for general public exposure [65]. The study revealed reduced body weight of both male and female pups and low but significant incidences of malignant gliomas in the brain and schwannomas in the heart of male rats [66]. Follow-up assessments from this study revealed significant DNA damage in the brain and peripheral blood leukocytes of rats and mice [67]. This, and a limited number of other mammal-based studies [61] suggest that developmental exposures to RFR can result in adverse effects. However, there also exists evidence to the contrary, with several epidemiological studies suggesting a lack of effects unequivocally attributable to RFR exposure [68]. Most of the published RFR studies are based on previous generations of telecommunication RFRs. With the advent of 5G RFR exposures from mobile phones and other near proximity devices such as Wi-Fi routers and IoT appliances, public concerns about the safety of these high frequency exposures is likely to increase. This will also lead to a plethora of pseudoscience and well-meaning but poorly informed opinion. Thus, good science in the form of carefully controlled studies aimed at non-thermal effects and mechanisms of higher frequency RFR exposures are necessary and timely.

Since RFR exposures are not chemical in nature, the potential biological mechanisms and targets are expected to be very different from what we are more familiar with, but also readily translatable. For example, chemical receptor mechanisms with species-specific variation in receptor structure or downstream signaling processes may limit the translation of toxicological data across species. Because RFR exposures are electromagnetic radiation, one would expect non-thermal toxicological results, if they exist, to also be operant in humans. In this study, we used zebrafish as a surrogate model to study how RFRs might affect early development. Zebrafish constitutes an ideal model for this study since 1) they undergo rapid development, accomplishing primary organogenesis within 48 h post fertilization, 2) their ex utero development greatly facilitates monitoring abnormalities and examination of temporal windows of sensitivity to a stressor 3) RFR exposures of hundreds of embryos can be done uniformly in a multi-well plate inside a small Faraday cage built for contained RFR exposures [69]. Previous studies have assessed the effects of RFR on adult zebrafish. In one study, 2300 MHz 4G RFR (estimated SAR of 0.004 W/Kg) exposure from close proximity to a mobile phone was associated with altered patterns of locomotor activity that were dependent on both time of exposure (morning vs. evening) and duration of exposure, suggesting that RFR affected circadian rhythm [70]. In another study, a 14-day exposure to RFR from a mobile phone emitting 900 MHz (estimated SAR of 0.004 W/Kg) by playing 1 h of music daily via a call from another phone resulted in neurobehavioral and social deficits in adult fish; these effects were also associated with oxidative stress in brain tissues [71]. Overall, these studies suggested that relatively low dose RFR exposures altered neurobehavioral patterns in adult zebrafish. To our knowledge, only one study assessed the effects of developmental RFR exposures in zebrafish where exposure to 100 MHz RFR (SAR $\approx$ 0.04 W/Kg) from 0 to 72 h post fertilization (hpf) was associated with reduced growth, oxidative stress,

increased apoptosis and altered cholesterol path- way [72]. This suggests that vertebrate development may be impacted by RFR and that more research is needed to discover the developmental effects and targets of RFR. The advantages of the zebrafish model should enable rapid study of developmental stage sensitivity to varying RFR frequency and field strength, specifically GHz levels of RFR that define much of the existing and proposed cellular frequency spectrums. To achieve this, we standardized a plate based RFR exposure chamber and conducted a multi-part study assessing potential effects of continuous developmental exposure to high dose 3.5 GHz RFR, SAR $\approx$ 8.27 W/Kg. We used a trans- mission range of 60 mm through air and 5 mm through water. The 3.5 GHz frequency has been allocated by the US Federal Communications Commission (FCC) for wireless device manufacturers for the 5G spectrum [73] and is within a frequency range used by 4G and 5G bandwidths. This manuscript reports the first part of this systematic study where we used rapid screening to assess RFR-induced impacts on embryonic development and early life stage behavior.

5.2 Materials and methods

5.2.1 RFR exposure setup

The exposure chambers (both for RFR exposure and sham control exposure) consisted of in- house constructed 110 x 80 x 80 mm (L x W x H) Faraday cages made of 20-gauge copper plate with a tight-fitting lid made of the same material. Electrical continuity between the cage and lid was verified with an Ohm meter. The Faraday cages were sized to accommodate a 6 well microtiter plate. The RFR exposure chamber lid was fitted with a (model FR05-107) ultra-wide band, omnidirectional antenna with a 3.1–5 GHz

frequency range, 84% aver- age efficiency, measuring 10 x 10 x 0.8 mm in dimensions. The SMC bulkhead fitting at the antenna passed through the lid of the Faraday cage, insulated from the copper with a nylon sleeve around the SMC barrel and nylon washers behind the upper and lower mounting nuts. The Fractus antenna was thus centrally affixed 3 mm below the inside surface of the Faraday cage lid and was immobile. The sham control chamber was identical to the RFR exposure chamber, but without an antenna and served to shield against the impacts of background RFR present at the location of the experiment.

Fig. 5.1A and 5.1B show our experimental setup for RFR exposure where the signal was generated using a transmitter (Analog Devices, model ADRV9364-Z7020) connected to a power amplifier (PA) (Mini-circuits ZHL-42+). Using a spectrum analyzer (Tektronix RSA3408A) with a 30 dBm measurement threshold, we performed preliminary assessments to measure the output from the PA. With a transmitter output of -9 dBm at 3.5 GHz, the PA output was 26.7 dBm. During our experiments, we set the transmitter to an output of -6 dBm at 3.5 GHz and expected a PA output of 30–32 dBm signal power. The amplified signal was administered to the zebrafish embryos via SMC cable connection from the PA to antenna attached to the RFR chamber; the sham chamber did not receive any signal.

The incident power density of the zebrafish embryo exposures, at the water surface, was approximately 22 W/m^2. This estimate considered the reported signal power, a 6 cm distance ($\approx 0.2\lambda$) from the antenna and unity gain at the antenna for use in the equation:

$$P_D = \frac{P_o G_{tx}}{4\pi D^2} \tag{5.1}$$

Where: $P_D = W/\mathrm{m}^2; P_o$ = output W from antenna; G_{tx} = antenna gain; D = distance from the antenna in meters. Because of the high complexity in calculating the propagation path loss in near-field propagation cases such as this, we believe that in our small volume, highly reflective system, using the density equation provides sufficient insight.

To report the RFR exposures in more widely accepted health safety terms, we estimated the specific absorption rate (SAR) to be 8.27 W/Kg. SAR is defined as the rate at which RF energy is absorbed per unit mass, i.e., the 'dose rate' in watts per kilogram (W/kg) using the equation:

$$SAR = \frac{\sigma E^2}{m_d} \tag{5.2}$$

Where σ = conductivity of material (here zebrafish tissue, assumed isotonic with surrounding embryo medium which is approximately 1 $Siemen/\mathrm{m}$ conductivity); E = electric field in V/m, where the incident power density of 22 $\mathrm{W/m^2}$ (above) is equal to 91 $\mathrm{V/m}; \mathrm{m_d}$ = the mass density of embryonic zebrafish, estimated from wet embryo weight, at approximately $1\mathrm{mg/mm^3}$ or $1000\mathrm{Kg/m^3}$.

Each chamber accommodated a Cell MicroControls well plate heater (model HWPT-96) controlled remotely by an mTCII micro-temperature controller to maintain a constant $\sim 28°\mathrm{C}$ during embryonic development. The wire leads for the plate heater and thermistor probe passed through a small hole drilled on the short edge of the cage bottom just above the cage floor. The stack height (bottom to top) of cardboard thermal insulation, plate heater and the well plate was 25mm. For the RFR exposure chamber, the distance from the antenna face to the surface of the water column surface was consistently set at 60 mm. We note that 3.5GHz permittivity in a vacuum (dielectric constant 1 = perfect) vs. air are so similar that they are equal, for all practical purposes, over a 60 mm transmission range

(the higher the dielectric constant of a substance, the greater the signal attenuation). To reduce signal attenuation by the water component (1000μS/m conductivity, 28°C, thus dielectric constant $>$ 88 and attenuation at least 88 times that of air), the water depth above the embryos was limited to $\sim$ 5 mm, the minimum required to avoid potentially confounding effects of evaporation. Fig. 5.2 contains an image of the actual experimental setup.

5.2.2 Zebrafish husbandry

Adult Tropical 5D zebrafish were raised at Sinnhuber Aquatic Research Laboratory (SARL) at Oregon State University. The zebrafish were raised in standard laboratory conditions (28°C with 14 h light: 10 h dark photo cycle). Adult zebrafish were fed size appropriate Gemma Micro (Skretting Inc, Tooele, France) twice daily without supplementation of any live feed [74]. Adult care and reproductive techniques followed approved Institutional Animal Care and Use Committee protocol 5113 at Oregon State University.

5.2.3 Exposure regime

Embryos were collected in water from our recirculating system and sorted according to Kimmel et al 1995 [75]. All exposures and analyses were done based on our well-established high throughput pipeline (described in [76–79]), with some modifications. At $\sim$ 6hpf, embryos were bleached and transferred to 6 well flat-bottom plates (Falcon, Corning) with 50 embryos per well and 1 plate (6 wells) per treatment. The use of multiple embryos per well in a 6 well plate enabled the minimization of spatial variability of RFR exposure across different embryos that may be a concern for 96 well plates with one

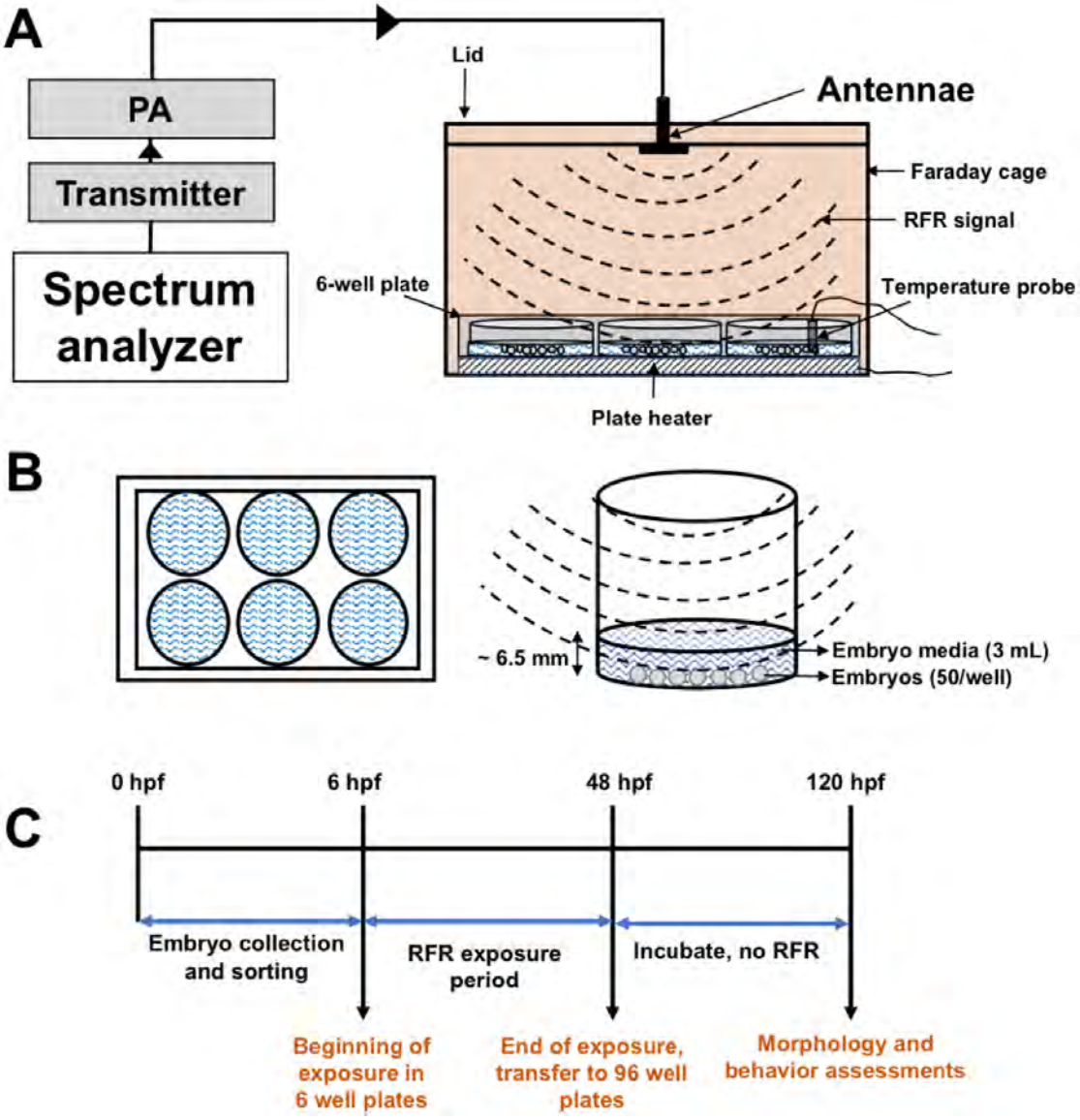

Figure 5.1: RFR embryonic exposure setup. (A) The transmitter generates RFR signal at 3.5 GHz that is amplified by the PA and broadcast in the Faraday cage via antenna. The Faraday cage contains a 6-well plate on a heating pad that maintains temperature of the plate at around 28°C. Each plate is fitted with a temperature probe to measure temperature of the EM. Arrows represent direction of current. An image of the actual setup is included in Fig. 5.2. (B) View of the 6-well plate from the top (left) and a magnified view of each well from the side (right). Each well contains 3 mL embryo media and 50 embryos. (C) Experimental flow chart, depicting start of exposure (6 hpf), end of exposure (48 hpf) and time of data acquisition (120 hpf).

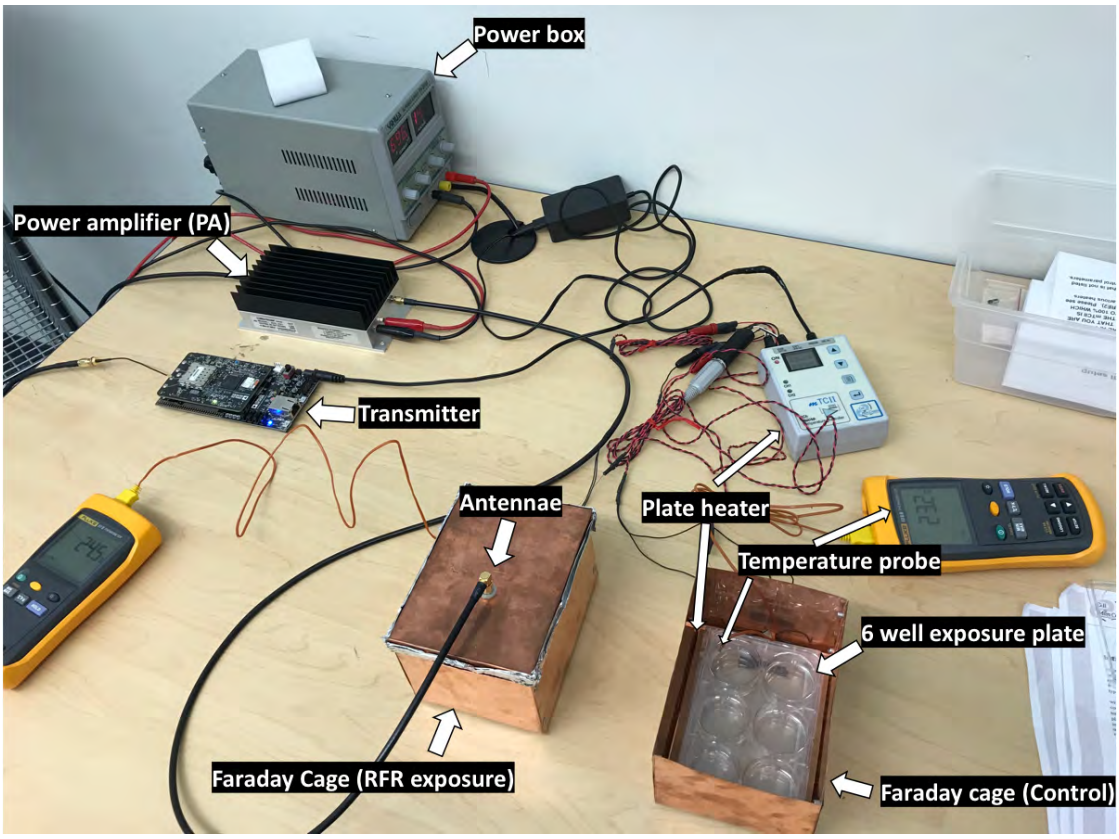

Figure 5.2: Image of the actual experimental setup.

embryo in each well typically used in our pipeline. Furthermore, plastic boundaries within each well of 96 well plates may also attenuate RFRs and distribute uneven signal into each well. All embryos were incubated in embryo media (EM), consisting of 15mM NaCl, 0.5mM KCl, 1mM MgSO, 0.15mM KH_2PO_4, 0.05mM Na_2HPO_4 and 0.7mM NaHCO3 [80]. The volume of EM in each well was minimized at 3mL to reduce RFR signal attenuation through the 5 mm water column above the embryos; preliminary observations showed that 50 embryos within this volume developed normally. To avoid evaporation, the plates were sealed with ThermaSeal RTS (polyolefin, 50μm thick) pressure-sensitive film and transferred to the temperature-controlled Faraday cages. A thermocouple temperature probe (Fluke, type K), remotely connected to a handheld thermometer (Fluke model 51–2), was placed into the water column of one well of each plate to serve as a secondary monitor of temperature independent of the thermistor probe attached to each well plate heater. RFR exposure was static, continued from 6–48 hpf and PA output were verified by spectrum analyzer. At 48 hpf, a subset of exposed embryos (N = 48, 8 embryos from each well of the 6 well plate to maintain representation of every well) were transferred into wells of a 96 well plate (1 embryo/well; prefilled with 100μL) for downstream assessments; no mortality or morphological defects were seen in embryos at 48 hpf. The 96 well plates were then sealed and incubated at 28°C in the dark for until 120 hpf when the plates were run through a battery of morphological and behavioral assessments (see below). The experiments were run thrice to capture the variability and to measure reproducibility; temperature and PA signal output remained stable and consistent throughout the experiments. Fig. 5.1C shows a flow chart representing our experimental paradigm.

5.2.4 Developmental toxicity assessments

At 120 hpf, mortality, morphology and behavioral endpoints were rapidly assessed; data for each treatment were combined from the 3 separate experiments N = 48 per experiment) resulting in N = 144. Seventeen developmental morphology endpoints included yolk sac edema (YSE) and pericardial edema (PE); body axis (AXIS), trunk length (TRUN), caudal fin (CFIN), pectoral fin (PFIN), pigmentation (PIG), and somite (SOMI) deformities; eye (EYE), snout (SNOU), jaw (JAW), and otolith (OTIC) malformations; gross brain development (BRAIN); notochord (NC) and circulatory (CIRC) deformities; swim bladder presence and inflation (SWIM); and touch-responses (TR). T he presence or absence of abnormality in each endpoint was entered into a laboratory information management system called the Zebrafish Acquisition and Analysis Program (ZAAP) [76]. Behavioral assessments consisted of the larval photomotor response assay and the larval startle response assay using the Viewpoint Behavior Technology ZebraBox and ZebraLab motion tracking (Viewpoint Life Sciences, Lyon, France) and stimulus triggering software; these were conducted just before morphological evaluation. For photomotor response, larvae experience a total of 3 light cycles, each cycle consisting of 3 min of alternating light and dark. The startle response assay consisted of an audible 100 dB, 600 Hz tone occurring for 900 ms, 30 seconds after the conclusion of the photomotor response assay (same instrument platform) with motion tracking commencing at the tone and for the following 9 seconds.

5.2.5 Statistical analyses

All statistical estimations were done within ZAAP which uses the R platform for analyses of various morphological and behavioral endpoints; details of analyses are described in our previous publications [77–79]. For mortality and morphology, statistical significance based on binary responses was computed as described in [77, 78]. Briefly, significant differences between control and exposed fish were computed using a one-sided Fisher's exact test, where adverse endpoints were tested to have a greater occurrence in exposed fish. For the photomotor response assay, an entropy score was calculated for each light phase interval and compared with the control group to compute a relative ratio, as described in [79]. For the startle response assay, the area under the curve (AUC) and peak response was calculated for the first startle only and compared to the first control startle response. This assay is performed in visible light. For both assays, statistical significance was determined using a Kolmogorov–Smirnov test ($p < 0.05$). For all behavioral assays, dead or severely deformed embryos were excluded from the analyses.

5.2.6 Results and discussion

The primary objective of this study was to assess whether exposure to high dose rate GHz frequency RFR is associated with any developmental perturbations during embryogenesis; this frequency range is expected to be widely deployed by major cellular services and hence most relevant for human exposures [73]. Importantly, we have created a microtiter plate-based for- mat for studying the impacts of RFR that can effectively replicate RFR exposures at different frequencies, field strengths and developmental windows. During the experiment (6–48 hpf), the temperature of the water medium for both controls

and RFR-exposed fish remained $\sim 28 - 29°C$, suggesting that, consistent with previous studies [72, 81], RFR exposures did not detectably increase water temperatures in the wells. Additionally, because of their small 1.5–2 mm size and composition, there is no reason to expect that zebrafish embryos would experience any net thermal flux beyond equilibrium with their environment. At 120 hpf, the RFR exposure did not lead to changes in mortality rate or incidences of abnormal morphology (Fig. 5.3A). These results are in contrast to a previous study that showed zebrafish embryonic exposure to 100 MHz RFR, estimated SAR ≈ 0.04 W/Kg, from 0–48 hpf resulted in developmental delays [72]. Disparate results between the two studies may be due to the time of exposure initiation (0 hpf in their study vs. 6 hpf in ours), since early developmental stages ($<$ 6 hpf) span early developmental events (cleavage, blastulation, gastrulation) that can be more sensitive to some stressors. Alternatively, because radio and micro-wave RFR penetration of tissues declines exponentially as frequency increases [64, 82], the 100 MHz exposure may have been substantially more bioactive than our 3.5 GHz exposure. The RFR exposures did not alter the photomotor response, in either the light or the dark phases (Fig. 5.3A and 5.3B). In the startle response assay, while the areas under the curve between control and RFR exposed groups were not significantly different, the RFR exposure did modestly reduce the peak height (peak swim distance); the acoustic startle was $\sim 16.5\%$ lower in the RFR exposed groups com- pared to the controls ($p = 0.045$) (Fig. 5.3A and 5.3C). The startle response is primarily driven by a sensorimotor response to acoustic cues and has been widely used to detect learning deficiencies in humans and to screen for neuroactive drugs in zebrafish [83, 84]. Suppression of startle response is indicative of depressed sensorimotor function which may result in adverse effects on neurobehavioral during post-developmental stages.

Overall, our results did not reveal any large-scale effects of RFR exposure on embryonic

survival or development but did reveal a modest depression of sensorimotor function. The possibility remains that developmental RFR exposures may produce molecular or later life stage effects not evaluated in this initial study. For example, the subtle startle response effect could be an early indicator of adult neuropsychiatric outcomes, like those detected in previous RFR studies [62]; though we note that published data suggesting non-thermal RFR effects associated with the low Hz (extreme low frequency; ELF) range is generally more conclusive than the published data suggesting non-thermal effects from exposure to the high MHz—low GHz range. It is also possible that 3.5 GHz RFR at a SAR of 8.27 W/Kg simply does not interact with and perturb normal vertebrate development. The combination of strong signal attenuation by the thin layer of EM (dielectric constant >88) over the embryos may have resulted in incident radiation density below the threshold for significant biological effects [81]. It is to be noted that we employed artificially high signal strength to maximize the likelihood of detecting RFR impacts; the 8.27 W/Kg SAR is approximately 200x larger than what a person using a mobile phone operating at mid-band 5G would be exposed to, and at least 100x larger than the basic limit for whole body exposure of 0.08 W/kg for general public exposure [65]. RFR tissue penetration is predicted from extensive modeling to be no more than about 6 mm at 3.5 GHz and rapidly declining to less than 1 mm in the upper 5G band and above [82]. The lack of large-scale effects at this high signal strength shows that a 3.5 GHz RFR is likely benign to users of devices usually emitting much lower signal strengths. Finally, it is possible that any RFR effects induced in our study may have been transient and the embryos may have recovered from or adapted to the static signal between the end of exposure (48 hpf) and experimental measurements (120 hpf). Future studies should employ longer continuous embryonic exposure periods with rapidly modulated frequencies to mimic mobile network signals. Our exposure platform also provides us an ideal setup for testing

higher frequency ranges, including the 5G-specific millimeter-wave range, in the future. In addition, we will also be able to study the compounding effects of RFR and other radiation types or chemical stressors on embryonic physiology.

5.3 Conclusion

Our study suggests that RFR, within the low GHz frequencies, is predominantly benign during embryonic development, but it may mildly depress sensorimotor functions when administered at a dose rate significantly higher than the general public exposure. This is the spectrum portion currently used for 4G LTE and 5G mid-band signals. Importantly, with this established, robust, in vivo testing platform, we are ideally positioned to model changing RFR exposures scenarios and measure their biological effects to address the concerns regarding broadband technology and human health.

5.4 Acknowledgments

The authors would like to thank members of the Tanguay Laboratory and the Sinnhuber Aquatic Research Laboratory, especially Carrie Barton, for their assistance with fish husbandry and chemical screening.

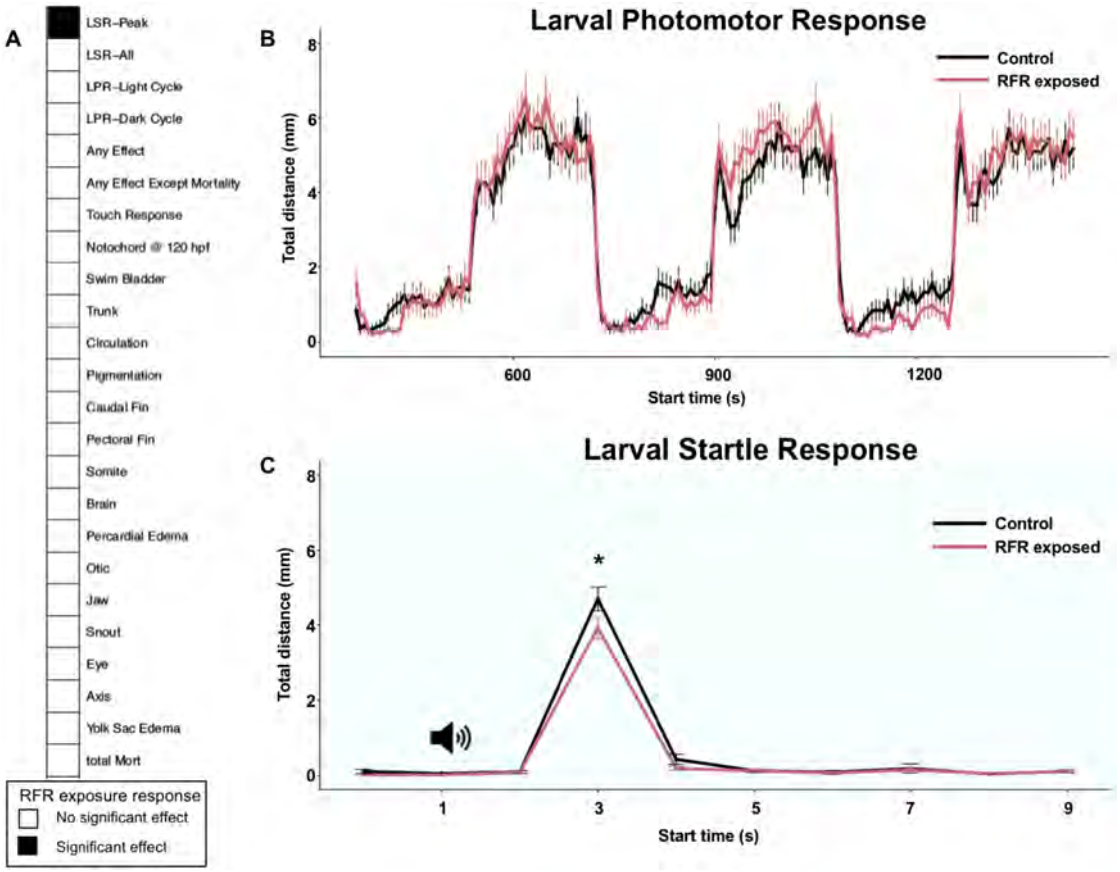

Figure 5.3: Effects of RFR on embryonic development. Embryos were exposed to 3.5 GHz, 30 dBm RFR, at a specific absorption rate (SAR) $\approx$ 8.27 W/Kg from 6–48 hpf and developmental parameters were measured at 120 hpf. All assays (panels A-C) were sequentially conducted from the same subset of embryos, with a total of 144 embryos from 3 replicate experiments used per treatment condition. (A) Summary of effects observed within our study. Measured parameters include mortality (Mort), 17 morphological parameters and 2 behavioral parameters (larval photomotor (LPR) and startle (LSR) responses). "Any effect" indicates a combination of all 17 morphological parameters. "LSR-All" indicates AUC and Peak measurements combined. (B) RFR exposure does not have any significant effect on photomotor response. (C) RFR exposure results in reduced peak height for startle response. Speaker icon denotes the acoustic signal. indicates a statistically significant difference at $p<0.05$.

Chapter 6: Conclusion and future works

6.1 Conclusion

This dissertation presents a set of studies, including RF channel model characterization, the design of a novel RF sensing system for indoor localization, and the environmental impact of RF exposure in such systems.

The first part covers a use case of measurement-based RF channel modeling in a challenging environment. The model is derived from actual S-parameter measurements using a connectorized mm-wave patch antenna. Path loss models, power delay profiles, and RMS delay spreads are obtained for both LOS and NLOS conditions. We focused on the feasibility of a mm-wave wireless link within a commercial server chassis for high data-rate links and for management and monitoring. Such servers have reflective metal walls and are densely populated with server boards that create barriers for mm-wave signals. A custom test setup is used for in-situ channel measurements at 57GHz for both line-of-sight (LOS) and non-line-of-sight (NLOS) links across different TX-RX separations. The NLOS links show RMS delay spread of 32ns@50% CDF (∼200ns@90% CDF) with path loss >55dB, indicating a challenging environment for low-power high-speed links. Therefore, a modified chassis with 10mm headroom between the top of the boards and chassis cover is proposed. Measurements show that such an environment can make the targeted wireless links feasible with ∼35dB loss, and RMS delay spread of 14ns@50% CDF (∼20ns@90% CDF).

The second part introduces an environment-adaptive RF sensing system for indoor

localization that consists of a dynamic phase calibration de-noising method, and the implementation of a localization system utilizes artificial neural network (ANN) with transferable features. In dynamic phase calibration de-noising method, two commodity wireless access points with built-in Atheros NIC were utilized for CSI phase extraction. A novel phase calibration method was proposed, which introduced two phase correction factors to improve the phase calibration process dynamically. A multi-layer neural network was trained to estimate the target's position. The results where evaluate both the prediction rate in an MoE model and the average position error illustrated that the use of the conventional linear transformation calibration method was suffered from a drop in prediction rate and, therefore, a lower position accuracy. For the CSI-based positioning system, the proposed method outperformed the conventional linear transformation calibration method by 13.2% higher prediction rate and reduces the average position error 21.3%.

In the implementation of a localization system utilizes artificial neural network (ANN), a novel domain adaptation scheme was proposed to estimate the position of an object in different environments. A WiFi-based platform was developed to access the real-time CSI through specialized OpenWrt firmware. A neural network model was designed for positioning and domain adaptation purposes. The model was trained by labeled CSI fingerprints from the source domain. Then, the transferable features of the CSI fingerprint between the source and the target domains are mapped into a common space during the domain adaptation process. A discriminator was utilized to detect the environmental changes and request a supplemental training set to recalibrate the adaptation process. The results showed the system adapted to environmental changes within the same test site when a large obstacle was blocking the area. Although it came at the cost of a lower predicted rate and positioning accuracy, with additional adaptation data, the system was

able to transfer the feature knowledge from one room to another.

Lastly, a collaboration work that explores the potential impact of RF radiation and how RF exposure could affect human health. This study suggests that RFR, within the low GHz frequencies, is predominantly benign during embryonic development, but it may mildly depress sensorimotor functions when administered at a dose rate significantly higher than the general public exposure. This is the spectrum portion currently used for 4G LTE and 5G mid-band signals. Importantly, with this established, robust, in vivo testing platform, we are ideally positioned to model changing RFR exposures scenarios and measure their biological effects to address the concerns regarding broadband technology and human health.

6.2 Future works

In this dissertation, we discussed an environment-independent transfer learning network for WiFi CSI- based indoor positioning system, in combination with an adaptive CSI phase calibration module to dynamically improve the data preprocessing. Although this proposed system is state of the art, it requires implementation and further improvements. The correction factors of the dynamic phase calibration process are semi-defined via empirical values. The correction factors can be automatically adjusted based on prediction for a higher dynamic range of phase noises. The current domain adaptation model incorporates the unlabeled data from the fingerprint recalibration process. The supplement dataset acquired during adaptation training has to be labeled to improve transfer learning. In extreme cases, some samples can be assigned incorrectly. A confidence constraint or semantics alignment should be considered to exploit prior knowledge completely. When evaluating the performance of the positioning and domain adaptation

models, the same-sized test site and placement of the transmitter and receiver are used in two different rooms.While maintaining those conditions, the results reveal the impact of environmental changes, such as the different number of obstacles and the type of furniture (e.g., wooden vs. metallic).Other placements of transceivers and objects may affect the estimation performance, such as the distance between the transmitter and receiver and the direction and orientation of the object.Multiple subjects or personnel presenting in the same area can be another challenging objective.

Besides localization and positioning, human activity recognition (HAR) is another trending topic for WiFi-based RF sensing systems. As shown in Fig.1.1, the current study of environmental variation, sensor placement, and user movement regarding domain adaption and transfer learning can be applied to HAR applications through our proposed RF Sensing ANN Framework. In similar testing environments, we collected CSI samples for multiple human activities, including sitting, standing, walking, and turning. Initial analysis shows that the domain adaption mechanism and transfer learning network designed for indoor positioning systems work sustainably as a learning generalization layer for HAR proposes. However, the generalization layer is still open for further research of new strategies and techniques. Future work requires identifying application-independent factors related to the learning generalization across different RF sensing applications. For example, instead of incorporating prior knowledge of the classifier from PHY measurement, the measured RF data can be learned as feature vectors. The resemblance among those feature vectors can reveal new insights for learning generalization.

Bibliography

[1] X Wang, X Wang, and S Mao, "Rf sensing in the internet of things: a general deep learning framework", IEEE Communications Magazine **56**, 62–67 (2018).

[2] Y Ma, G Zhou, and S Wang, "Wifi sensing with channel state information: a survey", ACM Comput. Surv. **52**, 46:1–46:36 (2019).

[3] G Wang, K Zhan, T Kamgaing, R Khanna, H Liu, and A Natarajan, "Measurement-based channel modeling for mmwave wireless links in enclosed server platforms", in 2017 ieee radio and wireless symposium (rws) (2017), pp. 141–143.

[4] Z Yang, Z Zhou, and Y Liu, "From rssi to csi: indoor localization via channel response", ACM Comput. Surv. **46**, `10.1145/2543581.2543592` (2013).

[5] S Feldmann, K Kyamakya, A Zapater, and Z Lue, "An indoor bluetooth-based positioning system: concept, implementation and experimental evaluation.", in (Jan. 2003), pp. 109–113.

[6] A Alarifi, A Al-Salman, M Alsaleh, A Alnafessah, S Al-Hadhrami, MA Al-Ammar, and HS Al-Khalifa, "Ultra Wideband Indoor Positioning Technologies: Analysis and Recent Advances.", Sensors **16** (2016).

[7] R Ye, S Redfield, and H Liu, "High-precision indoor uwb localization: technical challenges and method", in, Vol. 2 (Oct. 2010), pp. 1–4.

[8] Z Hao, H Yan, X Dang, Z Ma, P Jin, and W Ke, "Millimeter-wave radar localization using indoor multipath effect", Sensors **22**, `10.3390/s22155671` (2022).

[9] M Carlberg, L Hedendahl, T Koppel, and L Hardell, "High ambient radiofrequency radiation in stockholm city, sweden", Oncol. Lett. **17**, 1777–1783 (2019).

[10] P Chiang, S Woracheewan, C Hu, L Guo, R Khanna, J Nejedlo, and H Liu, "Short-Range, Wireless interconnect within a Computing Chassis: Design Challenges", IEEE Design & Test of Computers **27**, 32–43 (2010).

[11] A Natarajan, SK Reynolds, MD Tsai, ST Nicolson, JHC Zhan, DG Kam, D Liu, YLO Huang, A Valdes-Garcia, and BA Floyd, "A Fully-Integrated 16-Element Phased-Array Receiver in SiGe BiCMOS for 60-GHz Communications", IEEE J. Solid-State Circuits **46**, 1059–1075 (2011).

[12] R Felbecker, W Keusgen, and M Peter, "Incabin Millimeter Wave Propagation Simulation in a Wide-Bodied Aircraft Using Ray-Tracing", in Proc. ieee vehicular tech. conf. (vtc) (2008), pp. 1–5.

[13] S Khademi, SP Chepuri, Z Irahhauten, GJM Janssen, and AJ van der Veen, "Channel Measurements and Modeling for a 60 GHz Wireless Link Within a Metal Cabinet", IEEE Trans. Wireless Commun. **14**, 5098–5110 (2015).

[14] T Rappaport, *Wireless Communications: Principles and Practice, 2nd edition*, 2nd ed. (Prentice Hall PTR, 2001).

[15] K Pahlavan and AH Levesque, *Wireless Information Networks* (Wiley-Interscience, Verizon Communications, 1995).

[16] N Moraitis and P Constantinou, "Measurements and Characterization of Wideband Indoor Radio Channel at 60 GHz", IEEE Trans. Wireless Comm. **5** (2006).

[17] MS Varela and MG Sanchez, "RMS delay and coherence bandwidth measurements in indoor radio channels in the UHF band", IEEE Trans. Vehicular Tech. **50**, 515–525 (2001).

[18] A Makki, A Siddig, M Saad, and C Bleakley, "Survey of wifi positioning using time-based techniques", Computer Networks **88**, 218–233 (2015).

[19] A Lim and K Zhang, "A robust rfid-based method for precise indoor positioning", in International conference on industrial, engineering and other applications of applied intelligent systems (Springer, 2006), pp. 1189–1199.

[20] T Qiao and H Liu, "Improved least median of squares localization for non-line-of-sight mitigation", IEEE Communications Letters **18**, 1451–1454 (2014).

[21] T Qiao and H Liu, "An improved method of moments estimator for toa based localization", IEEE Communications Letters **17**, 1321–1324 (2013).

[22] T Qiao, S Redfield, A Abbasi, Z Su, and H Liu, "Robust coarse position estimation for tdoa localization", IEEE Wireless Communications Letters **2**, 623–626 (2013).

[23] Y Zou, H Liu, and Q Wan, "An iterative method for moving target localization using tdoa and fdoa measurements", IEEE Access **6**, 2746–2754 (2018).

[24] Z Su, G Shao, and H Liu, "Semidefinite programming for nlos error mitigation in tdoa localization", IEEE Communications Letters **22**, 1430–1433 (2018).

[25] Y Zou and H Liu, "Semidefinite programming methods for alleviating clock synchronization bias and sensor position errors in tdoa localization", IEEE Signal Processing Letters **27**, 241–245 (2020).

[26] P Bahl and VN Padmanabhan, “Radar: an in-building rf-based user location and tracking system”, in Proceedings ieee infocom 2000. conference on computer communications. nineteenth annual joint conference of the ieee computer and communications societies (cat. no.00ch37064), Vol. 2 (2000), 775–784 vol.2.

[27] M Youssef and A Agrawala, “The horus wlan location determination system”, in Proceedings of the 3rd international conference on mobile systems, applications, and services, MobiSys ’05 (2005), pp. 205–218.

[28] P Kumar, L Reddy, and S Varma, “Distance measurement and error estimation scheme for rssi based localization in wireless sensor networks”, in 2009 fifth international conference on wireless communication and sensor networks (wcsn) (2009), pp. 1–4.

[29] Y Zhuo, H Zhu, H Xue, and S Chang, “Perceiving accurate csi phases with commodity wifi devices”, in Ieee infocom 2017 - ieee conference on computer communications (2017), pp. 1–9.

[30] A Bhartia, YC Chen, S Rallapalli, and L Qiu, “Harnessing frequency diversity in wi-fi networks”, in Proceedings of the 17th annual international conference on mobile computing and networking, MobiCom ’11 (2011), pp. 253–264.

[31] K Wu, J Xiao, Y Yi, D Chen, X Luo, and LM Ni, “Csi-based indoor localization”, IEEE Transactions on Parallel and Distributed Systems **24**, 1300–1309 (2013).

[32] Q Song, S Guo, X Liu, and Y Yang, “Csi amplitude fingerprinting-based nb-iot indoor localization”, IEEE Internet of Things Journal **5**, 1494–1504 (2018).

[33] J Xiao, K Wu, Y Yi, and LM Ni, "Fifs: fine-grained indoor fingerprinting system", in 2012 21st international conference on computer communications and networks (icccn) (2012), pp. 1–7.

[34] Y Chapre, A Ignjatovic, A Seneviratne, and S Jha, "Csi-mimo: indoor wi-fi fingerprinting system", in 39th annual ieee conference on local computer networks (2014), pp. 202–209.

[35] S Sen, B Radunovic, RR Choudhury, and T Minka, "You are facing the mona lisa: spot localization using phy layer information", in Proceedings of the 10th international conference on mobile systems, applications, and services, MobiSys '12 (2012), pp. 183–196.

[36] X Wang, L Gao, S Mao, and S Pandey, "Deepfi: deep learning for indoor fingerprinting using channel state information", in 2015 ieee wireless communications and networking conference (wcnc) (2015), pp. 1666–1671.

[37] X Wang, L Gao, and S Mao, "Phasefi: phase fingerprinting for indoor localization with a deep learning approach", in 2015 ieee global communications conference (globecom) (2015), pp. 1–6.

[38] Y Xie, Z Li, and M Li, "Precise power delay profiling with commodity wifi", in Proceedings of the 21st annual international conference on mobile computing and networking, MobiCom '15 (2015), pp. 53–64.

[39] Y Gu, A Lo, and I Niemegeers, "A survey of indoor positioning systems for wireless personal networks", IEEE Communications Surveys Tutorials **11**, 13–32 (2009).

[40] S Zhao and H Liu, "Transmitter-side multipath preprocessing for pulsed uwb systems considering pulse overlapping and narrow-band interference", IEEE Transactions on Vehicular Technology **56**, 3502–3510 (2007).

[41] S Zhao, P Orlik, AF Molisch, H Liu, and J Zhang, "Hybrid ultrawideband modulations compatible for both coherent and transmit-reference receivers", IEEE Transactions on Wireless Communications **6**, 2551–2559 (2007).

[42] QD Vo and P De, "A survey of fingerprint-based outdoor localization", IEEE Communications Surveys Tutorials **18**, 491–506 (2016).

[43] Halperin, "Tool release: gathering 802.11n traces with channel state information", SIGCOMM Comput. Commun. Rev. **41**, 53 (2011).

[44] Y Xie, Z Li, and M Li, "Precise power delay profiling with commodity wi-fi", IEEE Transactions on Mobile Computing **18**, 1342–1355 (2019).

[45] R Gao, H Wang, D Wu, K Niu, E Yi, and D Zhang, "A model based decimeter-scale device-free localization system using cots wi-fi devices", in, UbiComp '17 (2017), pp. 241–244.

[46] S Han, Y Li, W Meng, C Li, T Liu, and Y Zhang, "Indoor localization with a single wi-fi access point based on ofdm-mimo", IEEE Systems Journal **13**, 964–972 (2019).

[47] X Wang, L Gao, and S Mao, "Csi phase fingerprinting for indoor localization with a deep learning approach", IEEE Internet of Things Journal **3**, 1113–1123 (2016).

[48] Q Gao, J Wang, X Ma, X Feng, and H Wang, "Csi-based device-free wireless localization and activity recognition using radio image features", IEEE Transactions on Vehicular Technology **66**, 10346–10356 (2017).

[49] H Chen, Y Zhang, W Li, X Tao, and P Zhang, "Confi: convolutional neural networks based indoor wi-fi localization using channel state information", IEEE Access **5**, 18066–18074 (2017).

[50] M Long, Y Cao, J Wang, and MI Jordan, "Learning transferable features with deep adaptation networks", in, ICML'15 (2015), pp. 97–105.

[51] L Gong, W Yang, Z Zhou, D Man, H Cai, X Zhou, and Z Yang, "An adaptive wireless passive human detection via fine-grained physical layer information", Ad Hoc Networks **38**, 38–50 (2016).

[52] X Li, D Zhang, Q Lv, J Xiong, S Li, Y Zhang, and H Mei, "Indotrack: device-free indoor human tracking with commodity wi-fi", **1**, `10.1145/3130940` (2017).

[53] L Zhang and H Wang, "Device-free tracking via joint velocity and aoa estimation with commodity wifi", IEEE Sensors Journal **19**, 10662–10673 (2019).

[54] X Guo and N Ansari, "Localization by fusing a group of fingerprints via multiple antennas in indoor environment", IEEE Transactions on Vehicular Technology **66**, 9904–9915 (2017).

[55] Y Zheng, Y Zhang, K Qian, G Zhang, Y Liu, C Wu, and Z Yang, "Zero-effort cross-domain gesture recognition with wi-fi", in Proceedings of the 17th annual international conference on mobile systems, applications, and services, MobiSys '19 (2019), pp. 313–325.

[56] SJ Pan and Q Yang, "A survey on transfer learning", IEEE Transactions on Knowledge and Data Engineering **22**, 1345–1359 (2010).

[57] CL Russell, "5 g wireless telecommunications expansion: public health and environmental implications", Environmental Research **165**, 484–495 (2018).

[58] M Simkó and MO Mattsson, "5g wireless communication and health effects—a pragmatic review based on available studies regarding 6 to 100 ghz", International Journal of Environmental Research and Public Health **16**, 10.3390/ijerph16183406 (2019).

[59] RN Kostoff, P Heroux, M Aschner, and A Tsatsakis, "Adverse health effects of 5g mobile networking technology under real-life conditions", Toxicology Letters **323**, 35–40 (2020).

[60] I Gorpinchenko, O Nikitin, O Banyra, and A Shulyak, "The influence of direct mobile phone radiation on sperm quality", Cent. European J. Urol. **67**, 65–71 (2014).

[61] R Singh, R Nath, AK Mathur, and RS Sharma, "Effect of radiofrequency radiation on reproductive health", Indian J. Med. Res. **148**, S92–S99 (2018).

[62] ML Pall, "Microwave frequency electromagnetic fields (EMFs) produce widespread neuropsychiatric effects including depression", J. Chem. Neuroanat. **75**, 43–51 (2016).

[63] AB Miller, ME Sears, LL Morgan, DL Davis, L Hardell, M Oremus, and CL Soskolne, "Risks to health and well-being from radio-frequency radiation emitted by cell phones and other wireless devices", Front. Public Health **7**, 223 (2019).

[64] L Gherardini, G Ciuti, S Tognarelli, and C Cinti, "Searching for the perfect wave: the effect of radiofrequency electromagnetic fields on cells", Int. J. Mol. Sci. **15**, 5366–5387 (2014).

[65] International Commission on Non-Ionizing Radiation Protection (ICNIRP), "Health issues related to the use of hand-held radiotelephones and base transmitters. in-

ternational commission on Non-Ionizing radiation protection", Health Phys. **70**, 587–593 (1996).

[66] M Wyde, M Cesta, C Blystone, S Elmore, P Foster, M Hooth, G Kissling, D Malarkey, R Sills, M Stout, N Walker, K Witt, M Wolfe, and J Bucher, "Report of partial findings from the national toxicology program carcinogenesis studies of cell phone radiofrequency radiation in hsd: sprague dawley® sd rats (whole body exposures)", bioRxiv, 10.1101/055699 (2018).

[67] SL Smith-Roe, ME Wyde, MD Stout, JW Winters, CA Hobbs, KG Shepard, AS Green, GE Kissling, KR Shockley, RR Tice, JR Bucher, and KL Witt, "Evaluation of the genotoxicity of cell phone radiofrequency radiation in male and female rats and mice following subchronic exposure", Environ. Mol. Mutagen. **61**, 276–290 (2020).

[68] KH Choi, M Ha, EH Ha, H Park, Y Kim, YC Hong, AK Lee, J Hwa Kwon, HD Choi, N Kim, S Kim, and C Park, "Neurodevelopment for the first three years following prenatal mobile phone use, radio frequency radiation and lead exposure", Environ. Res. **156**, 810–817 (2017).

[69] PD Noyes, GR Garcia, and RL Tanguay, "Advances in the use of zebrafish in developmental toxicology: linking genetics, behavior, and high-throughput testing strategies", in (2018).

[70] S Malik, AK Pati, and A Parganiha, "Short- and long-duration exposures to cell-phone radiofrequency waves produce dichotomous effects on phototactic response and circadian characteristics of locomotor activity rhythm in zebrafish, danio rerio", Biological Rhythm Research **52**, 1560–1575 (2021).

[71] A Nirwane, V Sridhar, and A Majumdar, "Neurobehavioural changes and brain oxidative stress induced by acute exposure to GSM900 mobile phone radiations in zebrafish (danio rerio)", Toxicol. Res. **32**, 123–132 (2016).

[72] CC Piccinetti, A De Leo, G Cosoli, L Scalise, B Randazzo, G Cerri, and I Olivotto, "Measurement of the 100 MHz EMF radiation in vivo effects on zebrafish d. rerio embryonic development: a multidisciplinary study", Ecotoxicol. Environ. Saf. **154**, 268–279 (2018).

[73] JM Moskowitz, "5g wireless technology: millimeter wave health effects", Electromagnetic Radiation Safety (2017).

[74] CL Barton, EW Johnson, and RL Tanguay, "Facility design and health management program at the sinnhuber aquatic research laboratory", Zebrafish **13 Suppl 1**, S39–43 (2016).

[75] CB Kimmel, WW Ballard, SR Kimmel, B Ullmann, and TF Schilling, "Stages of embryonic development of the zebrafish", Dev. Dyn. **203**, 253–310 (1995).

[76] L Truong, DM Reif, L St Mary, MC Geier, HD Truong, and RL Tanguay, "Multidimensional in vivo hazard assessment using zebrafish", Toxicol. Sci. **137**, 212–233 (2014).

[77] L Truong, D Mandrell, R Mandrell, M Simonich, and RL Tanguay, "A rapid throughput approach identifies cognitive deficits in adult zebrafish from developmental exposure to polybrominated flame retardants", Neurotoxicology **43**, 134–142 (2014).

[78] DM Reif, L Truong, D Mandrell, S Marvel, G Zhang, and RL Tanguay, "High-throughput characterization of chemical-associated embryonic behavioral changes predicts teratogenic outcomes", Arch. Toxicol. **90**, 1459–1470 (2016).

[79] G Zhang, L Truong, RL Tanguay, and DM Reif, "A new statistical approach to characterize chemical-elicited behavioral effects in high-throughput studies using zebrafish", PLoS One **12**, e0169408 (2017).

[80] M Westerfield, *The zebrafish book: a guide for the laboratory use of zebrafish (danio rerio)* (Institute of Neuroscience, University of Oregon, 2007).

[81] D Lee, J Lee, and I Lee, "Cell phone-generated radio frequency electromagnetic field effects on the locomotor behaviors of the fishes poecilia reticulata and danio rerio", Int. J. Radiat. Biol. **91**, 843–850 (2015).

[82] T Wu, TS Rappaport, and CM Collins, "The human body and millimeter-wave wireless communication systems: interactions and implications", in 2015 ieee international conference on communications (icc) (2015), pp. 2423–2429.

[83] RM Colwill and R Creton, "Imaging escape and avoidance behavior in zebrafish larvae", Rev. Neurosci. **22**, 63–73 (2011).

[84] RA Tegelenbosch, LP Noldus, MK Richardson, and F Ahmad, "Zebrafish embryos and larvae in behavioural assays", Behaviour **149**, 1241–1281 (2012).